

# Magnons from time-dependent density-functional perturbation theory and the noncollinear Hubbard formulation

Luca Binci<sup>1,2,3,\*</sup>, Nicola Marzari<sup>1,4</sup>, and Iurii Timrov<sup>4,+</sup>

<sup>1</sup>Theory and Simulation of Materials (THEOS), and National Centre for Computational Design and Discovery of Novel Materials (MARVEL), École Polytechnique Fédérale de Lausanne, CH-1015 Lausanne, Switzerland

<sup>2</sup>Department of Materials Science & Engineering, University of California Berkeley, Berkeley, CA, 94720, USA

<sup>3</sup>Materials Sciences Division, Lawrence Berkeley National Laboratory, Berkeley, CA, 94720, USA

<sup>4</sup>Center for Scientific Computing, Theory, and Data, Paul Scherrer Institut, 5232 Villigen PSI, Switzerland

\*Email: lbinci@berkeley.edu

+Email: iurii.timrov@psi.ch

## ABSTRACT

Spin excitations play a fundamental role in understanding magnetic properties of materials, and have significant technological implications for magnonic devices. However, accurately modeling these in transition-metal and rare-earth compounds remains a formidable challenge. Here, we present a fully first-principles approach for calculating spin-waves spectra based on time-dependent (TD) density-functional perturbation theory (DFPT), using Hubbard functionals in a noncollinear formulation. Unlike methods that rely on empirical Hubbard  $U$  parameters to describe the ground state, and Heisenberg Hamiltonians for describing magnetic excitations, the methodology developed here probes directly the dynamical spin susceptibility (efficiently evaluated with TDDFT through the Liouville-Lanczos approach), and treats the linear variation of the Hubbard augmentation (in itself calculated non empirically) in full at a self-consistent level. We benchmark the novel computational scheme on prototypical transition-metal monoxides NiO and MnO, showing remarkable agreement with experiments and highlighting the pivotal role of these newly implemented Hubbard corrections. The method holds great promise for describing collective spin excitations in complex materials containing localized electronic states.

## INTRODUCTION

In recent years, several intriguing research directions in spin excitations have attracted much attention; notably, these include magnonics in two-dimensional materials<sup>1,2,3</sup>, magnons in altermagnets<sup>4,5,6,7</sup>, and the coupling of magnons with other quasiparticles like excitons<sup>8,9</sup>, phonons<sup>10,11,12,13</sup>, and plasmons<sup>14,15,16</sup>. These phenomena often occur in complex materials containing magnetic transition-metal and/or rare-earth ions, and characterized as Mott-Hubbard or charge-transfer insulators<sup>17</sup>. While there have been many experimental breakthroughs in studying collective spin excitations (spin waves)<sup>18,19,20,21,22</sup>, theoretical and computational investigations remain challenging. To model the ground state of this class of materials, density-functional theory (DFT)<sup>23,24</sup> or the Korringa-Kohn-Rostocker (KKR) Green's function

method<sup>25,26</sup> are typically used. As it is well known, in DFT the choice of the exchange-correlation (xc) function is crucial. While standard local spin-density approximation (LSDA) and spin-polarized generalized-gradient approximation ( $\sigma$ -GGA) provide satisfactory results for itinerant magnetic metals, they are inaccurate for transition-metal and rare-earth insulating compounds due to strong self-interaction errors (SIEs) for partially filled and localized  $d$  and  $f$  electrons<sup>27,28</sup>. To address these challenges, more advanced functionals have been developed, among which Hubbard-corrected DFT functionals (DFT +  $U$ )<sup>29,30,31</sup> stand out for their capability to correct SIEs<sup>32,33</sup> and low computational cost. The value of Hubbard  $U$  is critical, and empirical tuning of  $U$  based on experimental results is a popular strategy; still, not only it requires accurate reference data, which are not always available,

but its transferability to properties that are often not fitted is debatable. To overcome these limitations, several first-principles approaches to compute  $U$  have been developed, including constrained DFT (cDFT)<sup>34,35,36,37,38,39,40</sup>, Hartree-Fock-based methods<sup>41,42,43,44,45,46</sup>, and the constrained random phase approximation (cRPA)<sup>47,48,49,50</sup>. Machine learning techniques for determining Hubbard parameters have also emerged in recent years<sup>51,52,53,54,55</sup>, which provide a fast and attractive route. The linear-response formulation of cDFT<sup>56</sup> has gained widespread popularity due to its simplicity and accuracy, and its recent reformulation using density-functional perturbation theory (DFPT)<sup>57,58,59</sup> has further enhanced its success. The physical rationale behind the linear-response determination of  $U$  relies on the heuristical imposition of piecewise linearity of the total energy of the system as a function of the occupation of the target Hubbard manifold<sup>56</sup>. Investigations of various magnetic materials using  $U$  from DFPT have proven to be accurate and effective<sup>60,61,62,63,64,65,66,67,68</sup>, making it an appealing approach for the description of spin waves.

The theoretical modeling of spin waves (magnons) can in general be achieved using a wide array of methodologies. One of the most popular technique involves model spin Hamiltonians, particularly the Heisenberg model, which relies on the adiabatic assumption that the time scales of magnons and electrons differ enough to allow the local electronic structure to adapt to the presence of magnons. The Heisenberg Hamiltonian is parametrized with interatomic exchange interactions  $J$  and other magnetic interaction parameters; e.g., single-ion anisotropy and/or Dzyaloshinskii-Moriya (DM) interactions<sup>69</sup>. These parameters are often obtained empirically by fitting them to experimental magnon dispersions. From a theoretical perspective, they can also be calculated from first principles using established approaches such as total energy differences<sup>70</sup>, spin-spiral energy dispersions based on the generalized Bloch theorem<sup>71,72,73</sup>, and the infinitesimal-rotations method based on the magnetic force theorem<sup>74,75,76,77</sup>. Once the Heisenberg Hamiltonian parametrization is set, magnon dispersions are determined using linear spin-wave theory (LSWT)<sup>78,79,80</sup>. Mapping experimental magnon dispersions to lattice spin models has proven to be very effective, offering a valuable tool for investigating complex systems,

particularly magnetic surfaces<sup>81</sup> and skyrmions<sup>82</sup>. However, using Heisenberg Hamiltonians requires prior knowledge of the specific magnetic interactions to include, which can be problematic if no experimental data are available. Additionally, in complex systems, the large number of  $J$  parameters and weak DM interactions can introduce intricacies and ill-conditioning in the determination of these quantities.

An alternative approach for modeling spin waves is to calculate directly the electronic response to an external magnetic potential, by evaluating explicitly the spin-spin susceptibility tensor. Two popular strategies to tackle this task are time-dependent density-functional theory (TDDFT)<sup>83</sup> and many-body perturbation theory (MBPT)<sup>84</sup>. TDDFT equations are typically solved in the linear-response regime in the frequency domain, assuming a small external magnetic field perturbation, and can be addressed using Dyson<sup>85,86,87,88,89,90,91</sup>, Sternheimer<sup>92,93,94</sup>, or Liouville-Lanczos (LL)<sup>95</sup> approaches. The strong perturbation regime can be accessed by solving TDDFT equations using real-time propagation, which enables the modeling of ultrafast phenomena<sup>96</sup>. MBPT techniques, consisting in the solution of the Bethe-Salpeter equation on top of the LSDA or  $GW$  ground state, have been devised for modeling magnons<sup>97,98,99,8</sup> and generally yield a more accurate description of magnons compared to TDDFT (if the latter is used with adiabatic LSDA (ALSDA)), but they come with considerable computational costs. Improved versions of TDDFT embodying more advanced functionals are attractive because they could deliver accurate magnon predictions while preserving moderate computational costs. In this context, extending TDDFT to incorporate Hubbard  $U$  corrections has proven effective for absorption spectroscopy<sup>100,101,102</sup>, but this extension to the case of magnons has only been explored in Ref. 94 using empirical  $U$  values when solving the Sternheimer equation with a finite-difference scheme, making the approach not being entirely *ab initio*. Instead, a fully non empirical, first-principles Hubbard approach is highly desirable, with  $U$  computed using one of the aforementioned methods and treated self-consistently and efficiently when solving the TDDFT equations.

To achieve this, and the aforementioned limitations, we propose a first-principles methodology

for the evaluation of spin-fluctuation spectra which is based on time-dependent density-functional perturbation theory (TDDFPT)<sup>83</sup> with noncollinear Hubbard functionals<sup>59</sup> in a Liouville-Lanczos (LL) scheme<sup>103</sup>. The formulation is entirely non empirical: (i) the Hubbard  $U$  parameter is not arbitrarily adjusted, but is calculated using DFPT<sup>56,104,57</sup> simultaneously optimizing also the crystal structure in a well defined self-consistent protocol<sup>105,58</sup>, and (ii) the approach probes explicitly the dynamical spin susceptibility, that is linked to the experimentally measurable double-differential cross section, thus providing a direct comparison with experiments<sup>95</sup>. Besides avoiding any reference to the electronic empty states, as routinely done in DFPT<sup>106</sup>, the greatest advantage of the LL approach for step (ii) relies in the fact that a single linear-response calculation enables inexpensively the evaluation of a column of the spin susceptibility  $\chi_{\alpha\alpha'}(\mathbf{q},\omega)$  at a large number frequencies. This is a desirable feature – especially when the magnon spectrum of a material is not known *a priori* – because it allows a facile identification of the spin excitations along the frequency axis, without the need of scanning several values of  $\omega$ , which instead would be required in the Sternheimer approach<sup>92,93</sup>. The LL method was already successfully applied to optical absorption spectroscopy<sup>103,107</sup>, electron-energy loss spectroscopy<sup>108</sup>, and inelastic neutron scattering spectroscopy<sup>95</sup> (although limited to standard DFT functionals), and it includes the self-consistent readjustment of the charge and magnetization densities. In this work, we explicitly account for the first-order variation of the Hubbard potential, similarly to the static phonon DFPT implementation<sup>109,61</sup>. However, in the present noncollinear dynamical case we demonstrate that the linear response equation that is antiresonant with the external frequency  $\omega$  exhibits a reversal of the Hubbard magnetization – i.e. the magnetization projected onto the localized ( $3d$  or  $4f$ ) target manifold. Ultimately, the method proposed works directly with the linearization of the Kohn-Sham (KS) Bloch states in reciprocal space, and thus it bypasses intermediate post-processing steps like Wannierizations<sup>77,110,85</sup>, improving user-friendliness and automation.

We apply this novel framework to the study of the magnon dispersions of NiO and MnO. By consistently addressing the electronic, structural, and

magnetic degrees of freedom, we achieve a highly accurate determination of spin waves, comparable to results from more advanced methods like DMFT<sup>111</sup> or  $GW$ <sup>112,3</sup> but at much more moderate computational cost that will allow dealing with complex materials and large supercells. As a byproduct of the calculations, we fit the magnon dispersions in order to extract the exchange parameters, which are then used to explain features of the magnon dispersions, and link them to the different magnitude of the rhombohedral distortions detected in the two materials investigated. These structural distortions are shown to be correctly captured by the present approach, thanks to the use of an iterative evaluation of the Hubbard parameters and structural optimizations, yielding the self-consistent Hubbard  $U$  and crystal structure.

## RESULTS AND DISCUSSION

### Time-dependent density-functional perturbation theory with Hubbard corrections

TDDFPT is a dynamical generalization of static DFPT<sup>104,113</sup>, where the external perturbation is decomposed into monochromatic components characterized by  $\mathbf{q}$  wave-vectors<sup>95</sup>. Due to the frequency dependence, two first-order (Sternheimer) equations must be solved: one *resonant* with the perturbation frequency  $\omega$  at wave-vector  $\mathbf{q}$ , and one *antiresonant* with  $-\omega$  at wave-vector  $-\mathbf{q}$ . Different methods have been developed to handle these equations. For example, in Ref. 93 the antiresonant equation was explicitly solved at  $-\mathbf{q}$ , while Ref. 95 applied the time-reversal operator  $\hat{\mathcal{T}} = \iota\sigma_y\hat{K}$  (with  $\hat{K}$  being the complex-conjugate operator) to the antiresonant equation, which restores the positive sign of  $\omega$  and  $\mathbf{q}$  in the response quantities while reversing the sign of the magnetic xc potential  $\mathbf{B}_{xc}$ . The operator  $\hat{\mathcal{T}}$  has also been used in static DFPT to calculate phonons<sup>114</sup> and the Hubbard  $U$  parameter<sup>59</sup>. Given its formal elegance, in this work we follow this latter methodology.

The core of this paper is an extension of the TDDFPT formalism from Ref. 95 to noncollinear Hubbard functionals<sup>59</sup>. We present the general formalism for both metals and insulators using norm-conserving pseudopotentials, and we use Hartree atomic units. It is worth noting that extending the current formalism to ultrasoft pseudopotentials<sup>115</sup>

and the projector augmented wave method<sup>116</sup> is straightforward but rather involved<sup>117,118</sup>, and could be addressed in future work.

### Ground state

In a noncollinear DFT+ $U$  scheme, the Hubbard occupation is a  $2 \times 2$  matrix in spin space<sup>119,102,120</sup>. The implementation of this formalism supports Löwdin-orthogonalized pseudo-atomic orbitals, which define the localized Hubbard subspace of interest<sup>59</sup>. For spinorial quantities, we adopt the notation  $|\Psi_i\rangle = \sum_{\sigma} |\psi_i^{\sigma}, \sigma\rangle$  and  $|\Phi_m^I\rangle = \sum_{\sigma} |\phi_m^{I\sigma}, \sigma\rangle$  for the KS spinor and the Hubbard atomic states, respectively (see Ref. 59 for more detailed definitions). Here,  $i$  is the collective index for quasimomentum and KS band indices  $i = n\mathbf{k}$ ,  $I$  is the atomic site index,  $m$  is the magnetic quantum number, and  $\sigma$  is the spin index. The Hubbard occupation matrix is defined as  $N_{mm'}^I = \sum_i \tilde{\theta}_i \langle \Psi_i | \hat{P}_{m'm}^I | \Psi_i \rangle$ , where  $\tilde{\theta}_i$  are the electronic occupancies – which equal to 0 and 1 for empty and occupied states at zero temperature, respectively, and have intermediate values for metals around the Fermi level – and  $\hat{P}_{m'm}^I = |\Phi_m^I\rangle\langle\Phi_{m'}^I|$  is the projector on the Hubbard subspace. In spin-resolved components, the Hubbard occupation matrix reads:

$$N_{mm'}^{I\sigma\sigma'} = \sum_i \tilde{\theta}_i \langle \psi_i^{\sigma'} | \phi_{m'}^I \rangle \langle \phi_m^I | \psi_i^{\sigma} \rangle. \quad (1)$$

In terms of these quantities, the Hubbard energy is given by<sup>59</sup>:

$$E_U = \sum_{Im} \frac{U^I}{2} \text{Tr} \left( N_{mm}^I - \sum_{m'} N_{mm'}^I N_{m'm}^I \right), \quad (2)$$

where the trace (Tr) is taken over the spin degrees of freedom.

As was mentioned earlier, in order to exploit the time-reversal operator  $\hat{T}$  in the antiresonant Sternheimer equation, we need to determine how  $N_{mm'}^I$  and  $\hat{P}_{m'm}^I$  transform under time reversal. To this aim, we use the completeness property<sup>121</sup> of the Pauli matrices  $\boldsymbol{\sigma} = (\sigma^x, \sigma^y, \sigma^z)$ :  $\boldsymbol{\sigma}_{\zeta\zeta'} \cdot \boldsymbol{\sigma}_{\xi\xi'} = 2\delta_{\zeta\xi'}\delta_{\zeta'\xi} - \delta_{\zeta\zeta'}\delta_{\xi\xi'}$ , which allows to rewrite the occupation matrix (1) as<sup>59</sup>:

$$(N_{mm'}^I)^{\sigma\sigma'} = \frac{1}{2} \left( n_{mm'}^I \delta^{\sigma\sigma'} + \mathbf{m}_{mm'}^I \cdot \boldsymbol{\sigma}^{\sigma\sigma'} \right), \quad (3)$$

where  $n_{mm'}^I = \text{Tr}[N_{mm'}^I]$  and  $\mathbf{m}_{mm'}^I = \sum_{\sigma\sigma'} N_{mm'}^{I\sigma\sigma'} \boldsymbol{\sigma}^{\sigma\sigma'}$  are the Hubbard occupation

(or charge) and magnetization, respectively. In Eq. (3) and in the following, for the sake of convenience, we use a notation that explicitly highlights the dependence on the magnetization (indicated as a superscript in square brackets), which will be necessary later when we reverse the sign of the magnetization. From this representation, using the properties  $\hat{T}\hat{T}^{\dagger} = \hat{I}$  (where  $\hat{I}$  is the identity operator) and  $\hat{T}\boldsymbol{\sigma}\hat{T}^{\dagger} = -\boldsymbol{\sigma}$ , it follows that:

$$\begin{aligned} (\hat{T} N_{mm'}^I \hat{T}^{\dagger})^{\sigma\sigma'} &= \sum_{\sigma_1\sigma_2} \hat{T}^{\sigma\sigma_1} (N_{mm'}^I)^{\sigma_1\sigma_2} \hat{T}^{\dagger\sigma_2\sigma'} \\ &= (N_{m'm}^{I[-m]})^{\sigma\sigma'}, \end{aligned} \quad (4)$$

which is identical to Eq. (3) but with the opposite sign in front of the magnetization matrix  $\mathbf{m}_{mm'}^I$ . From this expression we can derive how the noncollinear Hubbard potential transforms under the time-reversal operation. Let us start from its definition<sup>59</sup>:

$$\hat{V}_U^{[m]} = \sum_{Imm'} \frac{U^I}{2} [\delta_{mm'} - 2N_{mm'}^I] |\Phi_m^I\rangle\langle\Phi_{m'}^I|, \quad (5)$$

where the notation  $\hat{V}_U^{[m]}$  has to be understood as a  $2 \times 2$  matrix operator in the spin space. Next, using Eq. (4), by inverting the dummy indices  $m$  and  $m'$ , and since the application of  $\hat{T}$  on  $\Phi$  is immaterial (due to the spin-averaging procedure<sup>59</sup>) the desired transformation is:

$$\begin{aligned} (\hat{T} \hat{V}_U^{[m]} \hat{T}^{\dagger})^{\sigma\sigma'} &= \sum_{\sigma_1\sigma_2} \hat{T}^{\sigma\sigma_1} (\hat{V}_U^{[m]})^{\sigma_1\sigma_2} \hat{T}^{\dagger\sigma_2\sigma'} \\ &= (\hat{V}_U^{[-m]})^{\sigma\sigma'}, \end{aligned} \quad (6)$$

which is identical to Eq. (5) but with  $N_{mm'}^I$  being replaced by  $N_{mm'}^{I[-m]}$ , which has been discussed above.

### Dynamical linear response

Let us consider now an external weak perturbation of the system due to the magnetic dynamical potential with a finite  $\mathbf{q}$  modulation. This potential is given by the interaction energy of the system of electrons with an external magnetic field<sup>95</sup>:  $V_{\text{ext}}^{[\mathbf{B}\omega\mathbf{q}]}(\mathbf{q}, \omega) = -\mu_B \boldsymbol{\sigma} \cdot \mathbf{B}_{\omega\mathbf{q}}$ . Hereafter, we indicate with  $B_{\omega\mathbf{q}}^{\alpha}$  the  $\alpha$  Cartesian component of the vector amplitude of the external magnetic field. Next, we use the Bloch sum expression for the Hubbard atomic-like states<sup>122,57</sup>:

$$|\Phi_{m\mathbf{k}}^s\rangle = \frac{1}{\sqrt{N_{\mathbf{k}}}} \sum_l e^{i\mathbf{k}\cdot\mathbf{R}_l} |\Phi_m^{ls}\rangle = \frac{e^{i\mathbf{k}\cdot\mathbf{r}}}{\sqrt{N_{\mathbf{k}}}} |\nu_{m\mathbf{k}}^s\rangle, \quad (7)$$

where  $\nu_{m\mathbf{k}}^s(\mathbf{r} + \mathbf{R}_l) = \nu_{m\mathbf{k}}^s(\mathbf{r}) \equiv \sum_{\sigma} \nu_{m\mathbf{k}}^{s\sigma}(\mathbf{r})|\sigma\rangle$  is the lattice-periodic spinorial part, and  $N_{\mathbf{k}}$  is the number of points in the  $\mathbf{k}$ -grid. Here, we used the notation  $I \equiv \mathbf{R}_l + \boldsymbol{\tau}_s \equiv l\mathbf{s}$ , so that  $s$  identifies the atomic position within the  $l$ th cell. Going over to the  $(\omega, \mathbf{q})$  space and differentiating with respect to the cartesian  $\alpha$ -component of  $\mathbf{B}_{\omega\mathbf{q}}$ , we get the linearized Hubbard potential:

$$\frac{d\hat{V}_{U,\mathbf{k}}^{[m]}}{dB_{\omega\mathbf{q}}^{\alpha}} = - \sum_{smm'} U^s \frac{dN_{mm'}^{s[m]}}{dB_{\omega\mathbf{q}}^{\alpha}} |\nu_{m\mathbf{k}+\mathbf{q}}^s\rangle \langle \nu_{m'\mathbf{k}+\mathbf{q}}^s|, \quad (8)$$

for which a transformation law similar to Eq. (6) applies:

$$\hat{\mathcal{T}} \frac{d\hat{V}_{U,-\mathbf{k}}^{[m]}}{dB_{-\omega-\mathbf{q}}^{\alpha}} \hat{\mathcal{T}}^{\dagger} = \frac{d\hat{V}_{U,\mathbf{k}}^{[-m]}}{dB_{\omega\mathbf{q}}^{\alpha}}. \quad (9)$$

We now exploit Bloch's theorem for the KS spinors:  $|\Psi_i\rangle \equiv |\Psi_{n\mathbf{k}}\rangle = \frac{e^{i\mathbf{k}\cdot\mathbf{r}}}{\sqrt{N_{\mathbf{k}}}} |u_{n\mathbf{k}}\rangle$ . In terms of the lattice-periodic spinorial part  $u_{n\mathbf{k}}(\mathbf{r} + \mathbf{R}_l) = u_{n\mathbf{k}}(\mathbf{r}) \equiv \sum_{\sigma} u_{n\mathbf{k}}^{\sigma}(\mathbf{r})|\sigma\rangle$ , the first-order response Hubbard occupation matrix in Eq. (8) is written in terms of a first-order standard and time-reversed response KS wavefunctions:

$$\begin{aligned} \frac{dN_{mm'}^{s[m]}}{dB_{\omega\mathbf{q}}^{\alpha}} = \frac{1}{N_{\mathbf{k}}} \sum_{n\mathbf{k}} & \left[ \langle u_{n\mathbf{k}} | \nu_{m'\mathbf{k}}^s \rangle \langle \nu_{m\mathbf{k}+\mathbf{q}}^s | \Delta_{\omega\mathbf{q}}^{\alpha} u_{n\mathbf{k}} \rangle \right. \\ & \left. + \langle \hat{\mathcal{T}} u_{n-\mathbf{k}} | \hat{\mathcal{T}} \nu_{m-\mathbf{k}}^s \rangle \langle \hat{\mathcal{T}} \nu_{m'-\mathbf{k}-\mathbf{q}}^s | \hat{\mathcal{T}} \Delta_{-\omega-\mathbf{q}}^{\alpha} u_{n-\mathbf{k}} \rangle \right], \end{aligned} \quad (10)$$

$$\left( \hat{H}_{\mathbf{k}+\mathbf{q}}^{[B_{\text{xc}}]} + \hat{V}_{U,\mathbf{k}+\mathbf{q}}^{[m]} - \epsilon_{n\mathbf{k}} - \omega \right) | \Delta_{\omega\mathbf{q}}^{\alpha} u_{n\mathbf{k}} \rangle = -\hat{\mathcal{P}}_{\mathbf{k}+\mathbf{q}} \left[ \frac{d\hat{V}_{\text{Hxc}}^{[B_{\text{xc}}]}}{dB_{\omega\mathbf{q}}^{\alpha}} + \frac{d\hat{V}_{U,\mathbf{k}}^{[m]}}{dB_{\omega\mathbf{q}}^{\alpha}} + \frac{d\hat{V}_{\text{ext}}^{[B_{\omega\mathbf{q}}]}}{dB_{\omega\mathbf{q}}^{\alpha}} \right] | u_{n\mathbf{k}} \rangle, \quad (11)$$

$$\left( \hat{H}_{\mathbf{k}+\mathbf{q}}^{[-B_{\text{xc}}]} + \hat{V}_{U,\mathbf{k}+\mathbf{q}}^{[-m]} - \epsilon_{n-\mathbf{k}} + \omega \right) | \hat{\mathcal{T}} \Delta_{-\omega-\mathbf{q}}^{\alpha} u_{n-\mathbf{k}} \rangle = -\hat{\Pi}_{\mathbf{k}+\mathbf{q}} \left[ \frac{d\hat{V}_{\text{Hxc}}^{[-B_{\text{xc}}]}}{dB_{\omega\mathbf{q}}^{\alpha}} + \frac{d\hat{V}_{U,\mathbf{k}}^{[-m]}}{dB_{\omega\mathbf{q}}^{\alpha}} + \frac{d\hat{V}_{\text{ext}}^{[-B_{\omega\mathbf{q}}]}}{dB_{\omega\mathbf{q}}^{\alpha}} \right] | \hat{\mathcal{T}} u_{n-\mathbf{k}} \rangle, \quad (12)$$

where  $\hat{\mathcal{P}}_{\mathbf{k}+\mathbf{q}}$  and  $\hat{\Pi}_{\mathbf{k}+\mathbf{q}} = \hat{\mathcal{T}} \hat{\mathcal{P}}_{-\mathbf{k}-\mathbf{q}} \hat{\mathcal{T}}^{\dagger}$  are the standard and time-reversed projectors onto the occupied manifold, which have a more complex expression for metallic systems<sup>123,104,95</sup>. Here,  $\hat{H}_{\mathbf{k}+\mathbf{q}}^{[B_{\text{xc}}]}$  is the ground-state Hamiltonian defined in Eq. (21) in Ref. 95, and  $\hat{H}_{\mathbf{k}+\mathbf{q}}^{[-B_{\text{xc}}]}$  is its analogue with the reversed sign of  $\mathbf{B}_{\text{xc}}$ , while  $\epsilon_{n\mathbf{k}}$  and  $\epsilon_{n-\mathbf{k}}$  are the ground-state KS energies. This Hamiltonian does not include the ground-state lattice-periodic Hubbard potential  $\hat{V}_{U,\mathbf{k}+\mathbf{q}}^{[m]}$ , which instead appears as a separate term in

where the scalar products between the lattice-periodic parts of the spinors are summed over the spin components:  $\langle u|\nu\rangle \equiv \sum_{\sigma} \langle u^{\sigma}|\nu^{\sigma}\rangle$ . Equation (10) is valid for finite  $\mathbf{q}$ , while for  $\mathbf{q} = \mathbf{0}$  there is an extra term for metallic systems proportional to the derivative of the occupations<sup>123,104</sup>  $\hat{\theta}$ . The implementation of TDDFPT+ $U$  does not currently support the case  $\mathbf{q} = \mathbf{0}$ ; hence, this term is omitted. Also, in Eq. (10) the prefactor  $\hat{\theta}_{n\mathbf{k}}$  does not occur due to the definition of the response KS wavefunctions for metallic systems<sup>123</sup>. Thanks to the relations:

$$\frac{dn_{mm'}^I}{dB_{\omega\mathbf{q}}^{\alpha}} = \text{Tr} \left[ \frac{dN_{mm'}^I}{dB_{\omega\mathbf{q}}^{\alpha}} \right]; \quad \frac{d\mathbf{m}_{mm'}^I}{dB_{\omega\mathbf{q}}^{\alpha}} = \sum_{\sigma\sigma'} \frac{dN_{mm'}^{I\sigma\sigma'}}{dB_{\omega\mathbf{q}}^{\alpha}} \boldsymbol{\sigma}^{\sigma'\sigma}$$

it is readily seen that the time-reversed part of Eq. (10) has an inverted sign for the Hubbard magnetization  $\mathbf{m}$ , similarly to what happens for the induced spin-resolved charge density<sup>114</sup> (in analogy to Eqs. (26) and (27) of Ref. 95). Finally, in Eq. (10) the resonant  $\Delta_{\omega\mathbf{q}}^{\alpha} u_{n\mathbf{k}}$  and the time-reversed antiresonant  $\hat{\mathcal{T}} \Delta_{-\omega-\mathbf{q}}^{\alpha} u_{n-\mathbf{k}}$  wavefunctions can be obtained by solving the two coupled Sternheimer equations, which represent the core methodological development of this work:

the equations above, and  $\hat{V}_{U,\mathbf{k}+\mathbf{q}}^{[-m]}$  is its analogue with the reversed sign for the Hubbard magnetization  $\mathbf{m}$ . Finally, the response Hartree and xc (Hxc), response Hubbard, and external potentials appear on the right-hand side of the equations above with the specified signs of  $\mathbf{B}_{\text{xc}}$ ,  $\mathbf{m}$  and  $\mathbf{B}_{\omega\mathbf{q}}$ . Equations (11) and (12) differ from analogues equations in Ref. 95 by the presence of the ground-state and response Hubbard potentials tuned by the magnitude of the Hubbard  $U$  parameter. In addition, the ground-state KS energies, wavefunctions, and spin-resolved charge density

are obtained from the DFT+ $U$  ground state. Therefore, by solving Eqs. (11) and (12) self-consistently it is possible to obtain magnon energies including the Hubbard corrections with full internal consistency.

In principles, the dynamical Sternheimer equations (11) and (12) can be solved at each frequency  $\omega$ ; this provides the response KS wavefunctions  $\Delta_{\omega\mathbf{q}}^\alpha u_{n\mathbf{k}}$  and the corresponding time-reversed ones  $\hat{\mathcal{T}}\Delta_{-\omega-\mathbf{q}}^\alpha u_{n-\mathbf{k}}$ . The evaluation of these quantities gives access to the dynamical response spin-charge density matrix operator, defined as:

$$\frac{d\hat{\rho}}{dB_{\omega\mathbf{q}}^\alpha} = \frac{1}{N_{\mathbf{k}}} \sum_{n\mathbf{k}} \left( |\Delta_{\omega\mathbf{q}}^\alpha u_{n\mathbf{k}}\rangle \langle u_{n\mathbf{k}}| + |\hat{\mathcal{T}}\Delta_{-\omega-\mathbf{q}}^\alpha u_{n-\mathbf{k}}\rangle \langle \hat{\mathcal{T}}u_{n-\mathbf{k}}| \right). \quad (13)$$

The knowledge of this latter gives a complete description of the magnetic linear response of the system to a magnetic external perturbation, inasmuch as it delivers the spin susceptibility tensor through:

$$\chi_{\alpha\alpha'}(\mathbf{q}, \omega) = \mu_B \text{Tr} \left[ \sigma_\alpha \frac{d\hat{\rho}}{dB_{\omega\mathbf{q}}^\alpha} \right]. \quad (14)$$

This dynamical Sternheimer approach was successfully employed in Refs. 92,93 to calculate magnons in elemental itinerant metallic magnets and in the context of lattice-dynamical properties<sup>124,125,126</sup>. However, the main disadvantage of this approach is its high computational cost coming from the need to solve these equations self-consistently for each value of the frequency  $\omega$ . To avoid this drawback, we employ to the LL approach<sup>127,95</sup>, that enables the determination of the target column of the spin susceptibility tensor along the  $\omega$  axis at once with a single linear response calculation. The technical details concerning the implementation of noncollinear Hubbard functionals within this methodology can be found in the Method section.

## Applications

In this section, we present the application of the TDDFPT+ $U$  implementation using the LL approach to the transition-metal monoxides NiO and MnO. We first discuss the structural and electronic properties of these materials using LSDA and LSDA+ $U$ , comparing them with experimental data. Next, we present the calculated magnon dispersions using TDDFPT and TDDFPT+ $U$  within

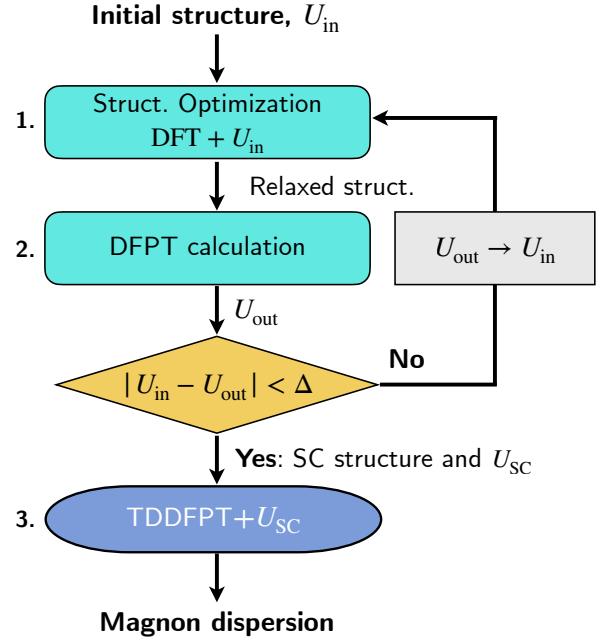


**Figure 1.** Computational protocol for the determination of the self-consistently (SC) optimized Hubbard  $U$  parameter, crystal structure, and magnon dispersion.  $U_{\text{in}}$ ,  $U_{\text{out}}$ , and  $U_{\text{SC}}$  are the input, output, and self-consistent Hubbard parameters, respectively, while  $\Delta$  is the convergence threshold.

ALSDA, and compare these results with experimental estimates. Finally, we extract the Heisenberg exchange interaction parameters by fitting the calculated magnon spectrum and compare them with experimental values. Both NiO and MnO are widely investigated antiferromagnetic (AFM) type II insulators. They crystallize in a rocksalt-type structure in the paramagnetic phase. Below their respective Néel temperatures, 524 K for NiO<sup>128</sup> and 120 K for MnO<sup>129</sup>, these materials exhibit a rhombohedral distortion along the [111] direction of the face-centered cubic (fcc) lattice.

We start our analysis by determining the electronic and the crystal structure of the ground state of NiO and MnO. The  $U$  parameter employed for the Hubbard augmentation part is calculated using linear-response theory<sup>56</sup>:

$$U^I = \left( \left[ \frac{dn_0^I}{d\lambda_{I'}} \right]^{-1} - \left[ \frac{dn^I}{d\lambda_{I'}} \right]^{-1} \right)_{II}, \quad (15)$$

where  $n^I \equiv \sum_m \text{Tr}(N_{mm}^I)$  and  $n_0^I \equiv \sum_m \text{Tr}(N_{0,mm}^I)$

Material	Method	$a$ (Å)	$\vartheta$ (deg)	$ \mathbf{m} $ ( $\mu_B$ )	$E_g$ (eV)
NiO	LSDA	4.93	33.97	1.15	0.48
	LSDA+ $U$	5.03	33.63	1.60	3.04
	Expt.	5.11 <sup>a</sup>	33.56 <sup>a</sup>	1.77 <sup>c</sup>	4.0 <sup>e</sup> 1.90 <sup>d</sup>
MnO	LSDA	5.07	35.66	3.86	0.65
	LSDA+ $U$	5.32	34.16	4.19	1.93
	Expt.	5.44 <sup>b</sup>	33.56 <sup>b</sup>	4.79 <sup>c</sup>	4.1 <sup>e</sup> 4.58 <sup>d</sup> 3.9±0.4 <sup>g</sup>

**Table 1.** Crystal and electronic structure properties of NiO and MnO as computed using LSDA, LSDA+ $U$ , and as measured in experiments. The equilibrium rhombohedral lattice parameter ( $a$ ), rhombohedral angle ( $\vartheta$ ), magnetic moment ( $|\mathbf{m}|$ ), and band gap ( $E_g$ ) are presented. The experimental values for  $a$  and  $\vartheta$  are determined from the cubic lattice using the experimental lattice parameter (4.17 and 4.43 Å for NiO<sup>a</sup> and MnO,<sup>b</sup> respectively), since experimentally the rhombohedral distortion is not reported. The angle  $\vartheta = 33.56^\circ$  corresponds to the case with no rhombohedral distortion. Ref.<sup>a</sup>: 130, Ref.<sup>b</sup>: 131, Ref.<sup>c</sup>: 132, Ref.<sup>d</sup>: 133, Ref.<sup>e</sup>: 134, Ref.<sup>f</sup>: 135, Ref.<sup>g</sup>: 136.

are the interacting and the noninteracting part, respectively, which are decomposed into monochromatic perturbation according to DFPT<sup>57,59</sup>:  $dn^I/d\lambda_{I'} = \frac{1}{N_q} \sum_{\mathbf{q}} e^{i\mathbf{q}\cdot(\mathbf{R}_I - \mathbf{R}_{I'})} \Delta_{\mathbf{q}}^{s'} n^s$  (detailed expression can be found in Refs. 57,58,59). Thanks to the collinearity of the AFM ground state, and the neglect of the spin-orbit coupling due to the lightness of the elements, it is safely possible to restrict such a calculation to the collinear case, thus saving substantial computational effort. In order to simultaneously optimize the Hubbard parameters and the crystal structure, we employed the workflow proposed in Refs. 105,58 and depicted in Fig. 1. This latter alternates variable-cell structural relaxations and determination of the  $U$  parameter until convergence is achieved. We obtained  $U$  of 6.26 and 4.29 eV for Ni-3d and Mn-3d states in NiO and MnO, respectively.

Table 1 summarizes the equilibrium rhombohedral lattice parameter ( $a$ ), rhombohedral angle ( $\vartheta$ ), magnetic moment ( $|\mathbf{m}|$ ), and band gap ( $E_g$ ) as computed

using LSDA, LSDA+ $U$ , and as measured in experiments (see also Fig. 5b). The experimental values for  $a$  and  $\vartheta$  are derived from the cubic lattice<sup>130,131</sup>. We are not aware of any direct experimental reports of the rhombohedral lattice parameters for these materials, possibly because the rhombohedral distortions are small and hard to resolve experimentally. Therefore, the comparison of our theoretical rhombohedral lattice parameters with the experimental reference values should be considered somewhat peripheral. It is found that the Hubbard correction systematically improves over LSDA. Still, nonnegligible discrepancies are present even in the LSDA+ $U$  approach, which are to a large extent due to the limitation of the base xc LSDA functional that is known to cause excessive binding in crystal structures. Improved estimates for  $a$ ,  $\vartheta$  and  $|\mathbf{m}|$  are expected if more advanced xc functionals are employed, for instance incorporating gradient or kinetic-energy density corrections like PBEsol<sup>137</sup> or SCAN<sup>138</sup>. Concerning  $E_g$ , although its value generally improves when Hubbard corrections are included (see e.g. Ref. 139), an underestimation of this quantity is to be expected, inasmuch as DFT+ $U$  is that theoretical framework that mainly corrects total energies. More precisely, when the band edges have the same orbital character of the Hubbard projectors, reasonable band gaps can be obtained with Hubbard-corrected functionals<sup>140,141,46</sup>. However, in the general case, for more accurate evaluations of spectral properties, methods like  $GW$ <sup>142,143,144</sup>, hybrid functionals<sup>145,146,147</sup> or Koopmans functionals<sup>148,149,150</sup> should be used.

Going over to the calculation of magnons, we recall that in the first Born approximation, there is a relation between the experimentally detectable double-differential cross section  $d^2\sigma/(d\Omega d\omega)$  (measuring the scattering of neutrons) and the spin susceptibility tensor  $\chi(\mathbf{q}, \omega)$  is given by:  $d^2\sigma/(d\Omega d\omega) = -\frac{g_n^2}{4\pi} \frac{k_f}{k_i} S(\mathbf{q}, \omega)$ <sup>151,152,95</sup>, where  $g_n$  is the neutron  $g$ -factor,  $k_i$  and  $k_f$  are the initial and final wavevectors of the scattered neutrons, and

$$S(\mathbf{q}, \omega) = -\text{Im Tr} \left( \mathbf{T}(\mathbf{q}) \chi(\mathbf{q}, \omega) \right), \quad (16)$$

where  $T_{\alpha\alpha'}(\mathbf{q}) = \delta_{\alpha\alpha'} - q_\alpha q_{\alpha'}/q^2$  is the projector to a plane transverse to the transferred momentum  $\mathbf{q}$ , and  $q = |\mathbf{q}|$ . The poles of  $S(\mathbf{q}, \omega)$  occur at the frequencies  $\omega(\mathbf{q})$  of magnons and Stoner excitations. To illustrate how the determination of the magnon

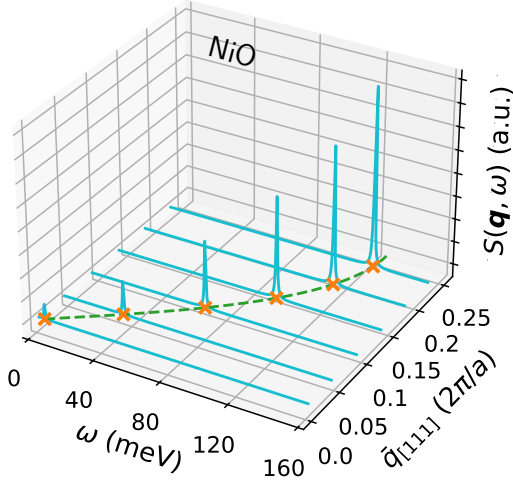


**Figure 2.**  $S(\mathbf{q}, \omega)$  (in cyan color) magnetic spectrum of NiO computed using TDDFPT+ $U$  using Eq. (16) as a function of the frequency  $\omega$  (in meV) at several values of the transferred momentum  $\mathbf{q}_{[111]} = (\bar{q} \bar{q} \bar{q})$  along the [111] direction (in units of  $2\pi/a$ , where  $a$  is the rhombohedral lattice parameter obtained from the distorted cell within LSDA+ $U$ ). Orange crosses mark the exact position of magnon peaks, and the green dashed line is a guide for the eye to highlight the magnon dispersion in the  $(\omega, \mathbf{q})$  plane.

spectrum is carried out, we report in Fig. 2 an example of the calculated  $S(\mathbf{q}, \omega)$  for different values of the transferred momenta  $\mathbf{q}$  for the magnon branch of NiO along the [111] direction. The sharp resonances in  $S(\mathbf{q}, \omega)$  indicate the frequency positions of the magnetic excitation of the system, which draw the spin-wave dispersions in the  $(\omega, \mathbf{q})$  plane. We also report in Fig. 3 the evolution of the average between the even and odd LL coefficients  $\alpha_n$  and  $\beta_n$  (see the Methods section) along the Lanczos chain (the coefficient  $\gamma_n$  is essentially equal to  $\beta_n$  and for conciseness we display only this latter). As it was reported in previous studies<sup>153,107,95</sup>, the  $\alpha_n$  coefficient is very small and oscillates around zero (when the batch rotation is performed, namely when time-reversal symmetry holds,  $\alpha_n = 0$  by construction<sup>103</sup>), while  $\beta_n$  is approximately equal to the half of the kinetic energy cutoff in the wavefunction expansion ( $\approx 40 = 80/2$  Ry). We mention that the number of LL iterations necessary to converge TDDFPT+ $U$  calculations is about 7000 – 8000, which is substantially smaller than the 16000 iterations needed to

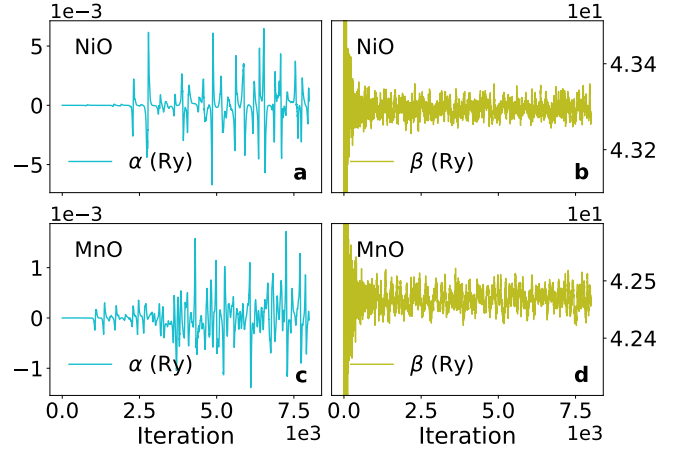


**Figure 3.** Behavior of the average even/odd Lanczos coefficients  $\alpha_n$  (panels a and c) and  $\beta_n$  (panels b and d) as a function of the number of Lanczos iterations  $n$  within TDDFPT+ $U$  for NiO and MnO.

converge TDDFPT. We attribute this difference to the fact that the + $U$  correction widens the band gap (see Table 1). As a consequence, the energy of the Stoner excitations is blue-shifted, and less electronic transitions contribute to the system’s response, stabilizing the convergence of the Lanczos chains.

In Fig. 4 we show the calculated magnon spectra for NiO and MnO with and without the Hubbard correction, and the comparison with experimental measurements<sup>154,155</sup>. Plain TDDFPT significantly overestimates the magnon energies with respect to experiments for both NiO and MnO. This aligns with previous LSDA-based theoretical studies<sup>111,112</sup>. On the contrary, the effect of the Hubbard augmentation is substantial, and it significantly improves agreement with experiments, not only for the amplitude of the magnon dispersion, but also for their curvature. This outcome is remarkable since the TDDFPT+ $U$  calculations are fully first-principles and do not rely on any empirical parametrization for the lattice parameters,  $U$  value, or type and/or strength of magnetic interactions. For MnO, we remark that the inclusion of the rhombohedral distortion is crucial in order to obtain a nonzero magnon energy at the  $M$  point<sup>73,156</sup>. For NiO instead the rhombohedral distortion is much smaller, resulting in a vanishing magnon energy at  $\mathbf{q} = M$ . We observe that it is important to account for the rhombohedral



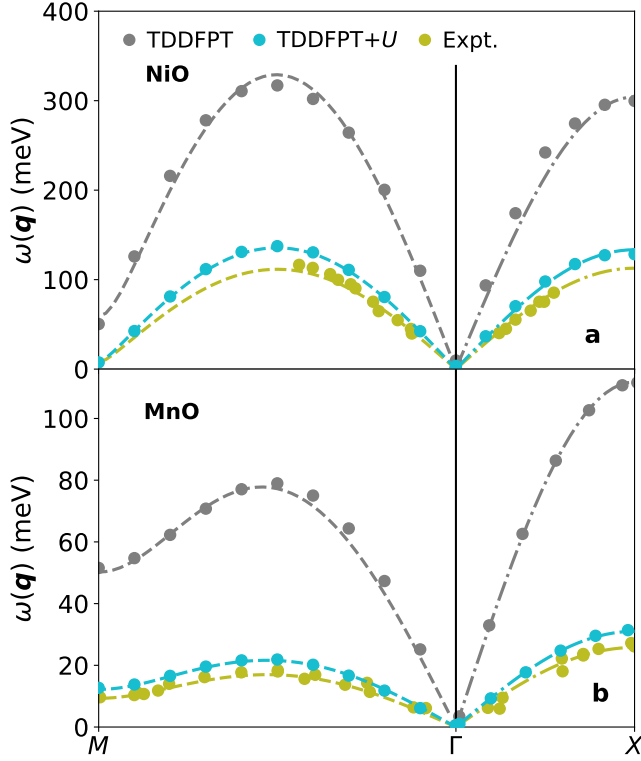


**Figure 4.** Magnon dispersions of (a) NiO and (b) MnO computed using TDDFPT (grey dots), TDDFPT+ $U$  (light blue dots), and as measured in experiments (olive dots)<sup>154,155</sup>. Dashed lines along  $\Gamma - M$  are fit using Eq. (18) with the parameters  $J_1^+$ ,  $J_1^-$ , and  $J_2$ , while the dash-dotted lines are fit along  $\Gamma - X$  using the simplified expression  $\omega_m^{[111]}(\mathbf{q})$  using  $\mathcal{J}$ . The values of the exchange parameters resulting from the fit are summarized in Table 2.

distortion within the selection of the  $\mathbf{q}$ -path across the Brillouine zone (BZ): the  $\Gamma - M$  high-symmetry direction undergoes a small rotation, while only the length along the  $\Gamma - X$  line is slightly modified. To do this, we specified the coordinates of the  $X$  and  $M$  points in the crystal framework (i.e., in the basis of the reciprocal lattice vectors of the BZ) and then transformed them to the Cartesian framework.

To gain further physical insights, we fit the magnon dispersions of Fig. 4 in order to have access to the Heisenberg exchange interactions parameters. For this analysis, we consider an Heisenberg model with nearest-neighbour (n.n.) and next-nearest-neighbour (n.n.n.) exchange interactions.

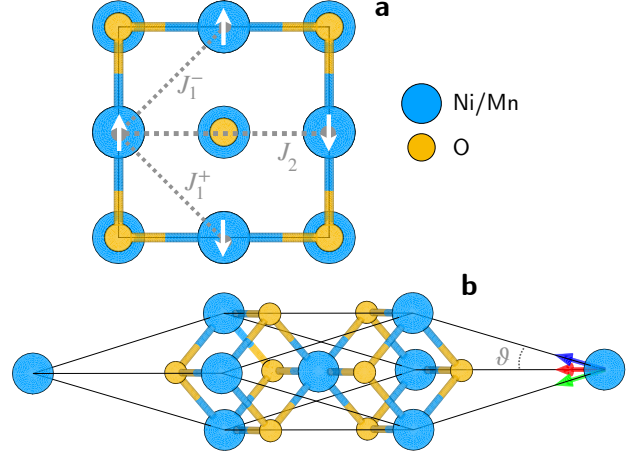


**Figure 5.** Schematic illustration of the NiO/MnO unit cell, showing the exchange interaction parameters  $J_1^+$ ,  $J_1^-$ , and  $J_2$  introduced in Eq. (17), and the angle  $\vartheta$  quantifying the rhombohedral distortion. Panel (a) shows the fcc cubic cell, while panel (b) displays the rhombohedral cell employed in our first-principles calculations.

The low-energy Hamiltonian reads<sup>155</sup>:

$$\hat{H} = \sum_{i,j}^{\text{n.n.p}} J_1^- \mathbf{S}_i \cdot \mathbf{S}_j + \sum_{i,j}^{\text{n.n.a}} J_1^+ \mathbf{S}_i \cdot \mathbf{S}_j + \sum_{i,j}^{\text{n.n.n.}} J_2 \mathbf{S}_i \cdot \mathbf{S}_j, \quad (17)$$

where the first sum is over nearest-neighbors with parallel spins ( $J_1^-$ ), the second sum is over nearest-neighbors with antiparallel spins ( $J_1^+$ ), and the third sum is over next-nearest-neighbors with antiparallel spins ( $J_2$ ) (see Fig. 5a). The notation  $J_1^-$  and  $J_1^+$ , introduced by Lines and Jones,<sup>157</sup> highlights the difference in interaction strength for nearest neighbors due to rhombohedral distortions<sup>158</sup>. Without these distortions,  $J_1^- = J_1^+$ . The Heisenberg Hamiltonian in Eq. (17) uses the same convention as in Ref. 155, assuming that more remote exchange interactions are negligible. We also neglect DM and single-ion anisotropy magnetic interactions in this Hamiltonian. Here,  $i$  and  $j$  label magnetic atomic sites, and  $\sum_{i,j}$  denotes the summation over pairs  $(i,j)$ .

From the Heisenberg Hamiltonian Eq. (17), using LSWT, it is possible to obtain an analytical expression for the magnon dispersion  $\omega(\mathbf{q})$  that explicitly depends on the exchange interaction parameters, which can then be used to fit the magnon spectrum in Fig. 4. The initial step involves transforming

Material	Method	$J_1^+$	$J_1^-$	$J_1$	$J_2$	$\mathcal{J}$	$ J_2/J_1 $	$\Delta J_1$	$ \Delta J_1/J_1  \times 100\%$
NiO	TDDFPT	-3.91	-4.21	-4.06	28.65	25.4	7.06	0.30	7.4%
	TDDFPT+ $U$	-0.90	-0.92	-0.91	11.60	11.1	12.75	0.02	2.2%
	Expt.	-0.68	-0.69	-0.69	9.50	9.40	13.77	0.01	1.4%
MnO	TDDFPT	1.39	0.81	1.10	1.89	3.73	1.72	0.58	52.7%
	TDDFPT+ $U$	0.54	0.40	0.47	0.53	1.03	1.13	0.14	29.8%
	Expt.	0.43	0.32	0.38	0.42	0.86	1.11	0.11	28.9%

**Table 2.** Exchange interaction parameters (in meV), using the convention for the Heisenberg Hamiltonian of Eq. (17), are extracted fitting the magnon dispersions of Fig. 4 using TDDFPT, TDDFPT+ $U$ , and experimental data from Refs. 154 and 155 for NiO (at 78 K) and MnO (at 4 K), respectively. Here,  $J_1 = (J_1^+ + J_1^-)/2$ , and  $\Delta J_1 = J_1^+ - J_1^-$ . The parameter  $\mathcal{J}$  has been fitted separately along the  $\Gamma \rightarrow X$  line, also for the experimental points.

the Hamiltonian to represent each spin within its local reference frame, oriented along the  $z$ -direction. Next, a Holstein-Primakoff transformation is performed<sup>80</sup>, replacing spin operators with creation and annihilation bosonic operators similar to those in a harmonic oscillator. During this transformation, the Hamiltonian is linearized, retaining terms up to the second order in the Holstein-Primakoff bosonic quasiparticles. Finally, the equation of motion is solved by diagonalizing the dynamical matrix, and a Bogoliubov transformation ensures a diagonalizing basis that adheres to the usual commutation relations. The final stage delivers the analytical expression for the magnon frequencies,  $\omega_m(\mathbf{q})$ . For a fcc lattice, this expression reads<sup>157</sup>:

$$\omega_m(\mathbf{q}) = \mu \sqrt{[J_{11}(\mathbf{q}) - J_{11}(\mathbf{0}) + J_{12}(\mathbf{0})]^2 - J_{12}(\mathbf{q})^2} \quad (18)$$

where  $\mu = 2S$ , i.e. it depends on the nominal magnetic moment  $S$  of the transition-metal ion ( $S = 1$  for  $\text{Ni}^{2+}$  and  $S = 5/2$  for  $\text{Mn}^{2+}$ ). The functions  $J_{11}(\mathbf{q})$  and  $J_{12}(\mathbf{q})$  are defined as<sup>154,155</sup>:

$$J_{11}(\mathbf{q}) = 2J_1^- \sum_{\alpha \neq \alpha'} \cos \pi(q_\alpha - q_{\alpha'}),$$

$$J_{12}(\mathbf{q}) = 2J_2 \sum_{\alpha} \cos(2\pi q_\alpha) + 2J_1^+ \sum_{\alpha \neq \alpha'} \cos \pi(q_\alpha + q_{\alpha'}).$$

In Fig. 4, we show the fit of the magnon dispersions of NiO and MnO from TDDFPT and TDDFPT+ $U$  using Eq. (18) along the  $\Gamma - M$  direction. Conversely, it is not possible to simultaneously determine all  $J_1^+$ ,  $J_1^-$ , and  $J_2$  parameters along the  $\Gamma - X$

direction (for which  $q_x = q_y = q_z = \bar{q}$ ). Indeed, by defining  $J_1$  as the average value,  $J_1 = (J_1^+ + J_1^-)/2$ , the analytical expression for the magnon dispersion reduces to:

$$\omega_m^{[111]}(\mathbf{q}) \approx 6\mathcal{J} \sin(2\pi\bar{q}). \quad (19)$$

where  $\mathcal{J} \equiv J_1 + J_2$ . This means that only the sum of the two exchange parameters ( $J_1$  and  $J_2$ ) can be extracted from the fit along the  $\Gamma - X$  direction, and not separately their individual values. Table 2 compares the theoretical Heisenberg exchange parameters obtained by fitting the TDDFPT and TDDFPT+ $U$  magnon dispersions in Fig. 4 with experimental values<sup>154,155</sup>. As shown in Table 2, the  $J_1^+$ ,  $J_1^-$ , and  $J_2$  parameters from TDDFPT within ALSDA are significantly overestimated compared to experimental values, while TDDFPT+ $U$  provides parameters much closer to experiments. Within TDDFPT, the theoretical exchange parameters deviate from the experimental ones by 150 – 500%, while within TDDFPT+ $U$  they deviate by 22 – 33%, with the sign of these parameters being correct in both cases, drastically improving the accuracy of the predictions. Given the strong dependence of the parameters  $J$  on the structural properties, we observe once again that the residual disagreement obtained with the Hubbard corrections could be further lowered by using more advanced xc functionals<sup>137,138</sup>. It would be possible to bring the theoretical exchange parameters even closer to experimental values by slightly increasing the  $U$  parameter<sup>73</sup>, but this would introduce an adjustable parameter and, by doing so, the theory would not be unbiased any-

more. This also highlights the strong sensitivity of the magnon dispersions and the corresponding  $J$  parameters to the value of the Hubbard  $U$ .

The difference between  $J_1^+$  and  $J_1^-$  serves as a useful measure of the impact of rhombohedral distortions on the magnon dispersions. We define  $\Delta J_1 = J_1^+ - J_1^-$ , and its relative strength compared to the average  $J_1$  parameter as  $|\Delta J_1/J_1|$ . Table 2 shows that  $\Delta J_1$  and  $|\Delta J_1/J_1|$  are in much closer agreement with the experimental values when using TDDFPT+ $U$  as compared to TDDFPT. When  $\Delta J_1 \rightarrow 0$ , the magnon energy at the  $M$  point in the BZ vanishes, as observed for NiO in Fig. 4, and which can be verified using Eq. (18). Increasing values of  $\Delta J_1$  lead to higher magnon energy at the  $M$  point, as it is showcased for MnO. This implies that  $\Delta J_1$  reflects the crystallographic inequivalence between two nearest-neighbor transition-metal ions, which is influenced by the rhombohedral distortion. Our first-principles calculations support this view, predicting a larger rhombohedral angle  $\vartheta$  (indicating greater rhombohedral distortion) for MnO compared to NiO (see Table 1). Consistently, LSDA, which overestimates  $\vartheta$  for both materials, displaying the largest values of both  $\Delta J_1$  and the magnon energy at the  $M$  point.

## CONCLUDING REMARKS

We have presented a first-principles approach for calculating magnons based on time-dependent density-functional perturbation theory<sup>95</sup> and the Liouville-Lanczos augmenting the adiabatic exchange-correlation functional with noncollinear Hubbard corrections. This Hubbard-extended formulation of TDDFPT is fully non empirical, since the Hubbard  $U$  parameter is computed from first-principles using DFPT<sup>57,59</sup>, avoiding any empirical calibrations. Additionally, the dynamical spin susceptibility tensor is directly computed through linear-response theory, without assumptions about the type and strength of magnetic interactions, unlike spin models such as the Heisenberg Hamiltonian. The Hubbard  $U$  correction is included self-consistently when solving the ground-state DFT+ $U$  problem, and its linear response is included when solving the TDDFPT+ $U$  equations using the LL approach. We chose the LL approach over the Dyson or Sternheimer methods because it is computationally efficient and provides access to all frequencies at once, unlike the point-

wise calculations required by the other methods. Similarly to the Sternheimer approach<sup>93</sup>, the LL approach avoids the computationally expensive summations over empty states<sup>95</sup>, commonly performed in static DFPT for phonons<sup>106</sup>. In all cases, the local spin density approximation (adiabatic in the time-dependent density-functional theory case) is used for the base exchange-correlation functional, then augmented with the Hubbard corrections.

To benchmark the TDDFPT+ $U$  formalism and ensure the correctness of its implementation, we applied it to the prototypical transition-metal monoxides NiO and MnO, including their rhombohedral lattice distortions. The computed magnon dispersions from TDDFPT+ $U$  show remarkable agreement with experimental data, unlike those from TDDFPT. Specifically, we accurately predict finite magnon energy at the  $M$  point in the BZ of MnO due to rhombohedral distortions, while this effect is negligible for NiO, consistent with experimental observations. Using the Heisenberg Hamiltonian and the LSWT, we fit the magnon dispersions to extract the nearest-neighbor and next-nearest-neighbor Heisenberg interaction parameters. The parameters obtained from TDDFPT+ $U$  align well with experimental values, whereas those from TDDFPT are largely overestimated. A detailed comparison of Heisenberg exchange parameters from TDDFPT+ $U$  and those calculated via total energy differences or the infinitesimal-rotations method is of great interest and is presented in a separate study<sup>159</sup>.

Although the current implementation of TDDFPT+ $U$  using the LL approach yielded good results, it still has limitations. Indeed, this approach is based on the linear-response regime, meaning it cannot simulate ultrafast phenomena with strong external perturbations<sup>96</sup>. Moreover, when solving the dynamical TDDFPT+ $U$  equations, the response Hubbard potential is computed using the static Hubbard  $U$  parameter, neglecting its dynamical variations due to external perturbations. We believe that this is a reasonable approximation since the external perturbation is assumed to be weak. Investigating the effect of dynamical modulation of  $U$  on magnons could be interesting, as done in Ref. 160 for studying high-harmonic generation. However, the  $U(\omega)$  parameter cannot be treated within the LL approach because it does not allow for a frequency-dependent response potential. To ex-

plore  $U(\omega)$ , switching to the Dyson or Sternheimer approaches would be necessary. On a more technical level, the current implementation is limited to LSDA, with  $\sigma$ -GGA currently unsupported, and it works only with norm-conserving pseudopotentials. Extensions to ultrasoft pseudopotentials<sup>115</sup> and the projector-augmented-wave (PAW) method<sup>116</sup> would be straightforward but they increase the computational complexity. In addition, the current implementation does not support symmetry yet, requiring the use of the full  $\mathbf{k}$  point grid in the BZ. We plan to implement symmetries in future versions of the TDDFPT+ $U$  code, which will further reduce the computational cost. Finally, the current implementation runs only on central processing unit (CPU) architectures, and porting it to graphics processing unit (GPU) architectures would significantly boost the speed of magnon calculations<sup>161,162</sup>.

Before concluding, we discuss the outlook and future prospects. Our TDDFPT+ $U$  implementation, based on Ref. 95, supports spin-orbit coupling (SOC). This is particularly relevant for heavy elements such as e.g. rare earths, containing localized  $f$  electrons requiring Hubbard corrections. Thanks to the noncollinear extension of DFT+ $U$  and DFPT<sup>59</sup>, it is possible to evaluate the Hubbard  $U$  parameter within the noncollinear framework, fully including SOC and further employ it within TDDFPT+ $U$ . Moreover, the current TDDFPT+ $U$  implementation can be straightforwardly extended to incorporate inter-site Hubbard  $V$  corrections<sup>141</sup>, that have proven to be very effective<sup>163,164,165,166,167,168,169,170</sup>. Additionally, the current TDDFPT+ $U$  implementation can be used for high-throughput calculations of magnons for hundreds or even thousands of materials using platforms like AiiDA<sup>171</sup>. This process can be further streamlined using equivariant neural networks to predict Hubbard parameters essentially at no cost, but with the accuracy close to that of DFPT<sup>54</sup>. We believe that the present TDDFPT+ $U$  extension opens the door to accurate modeling of magnons in complex transition-metal and rare-earth compounds, potentially leading to significant technological breakthroughs in spintronics and magnonics.

## METHODS

### *Liouville-Lanczos approach with Hubbard corrections*

The LL approach aims to solve the quantum Liouville spinorial equation, which is equivalent to the coupled dynamical Sternheimer equations (11) and (12). This is done by linearizing the Liouville equation, and taking advantage of the *batch representation*<sup>127,103,108</sup> to cast the equation in a matrix form that can be efficiently solved using the Lanczos algorithm<sup>172</sup>. The key advantage of using the LL approach over directly solving the dynamical Sternheimer equations is that the problem only needs to be solved once, regardless of frequency. The evaluation of the magnetic spectrum is then an inexpensive post-processing step<sup>173</sup>. The linearized quantum Liouville spinorial equation in the frequency domain reads<sup>95</sup>:

$$\frac{d\hat{\rho}}{dB_{\omega\mathbf{q}}^{\alpha}} = (\omega - \hat{\mathcal{L}}_{\mathbf{q}})^{-1} \left[ \frac{d\hat{V}_{\text{ext}}}{dB_{\omega\mathbf{q}}^{\alpha}}, \hat{\rho}_0 \right], \quad (20)$$

where  $\hat{\rho}_0$  is the ground-state spin-charge density matrix operator,  $d\hat{V}_{\text{ext}}/dB_{\omega\mathbf{q}}^{\alpha} \rightarrow d\hat{V}_{\text{ext}}^{[\pm B_{\omega\mathbf{q}}]}/dB_{\omega\mathbf{q}}^{\alpha}$  are the direct and reversed magnetic perturbations, and  $\hat{\mathcal{L}}_{\mathbf{q}} \rightarrow \hat{\mathcal{L}}_{\mathbf{q}}^{\pm}$  is the Liouvillian superoperator, which action over a generic quantum-mechanical operator  $\hat{X}$  is defined as:

$$\begin{aligned} \hat{\mathcal{L}}_{\mathbf{q}}^{\pm}(\hat{X}) \equiv & [\hat{H}^{[\pm B_{\text{xc}}]}, \hat{X}] + [\hat{V}_U^{[\pm m]}, \hat{X}] \quad (21) \\ & + \left[ \frac{d\hat{V}_{\text{Hxc}}^{[\pm B_{\text{xc}}]}}{dB_{\omega\mathbf{q}}^{\alpha}}, \hat{\rho}_0 \right] + \left[ \frac{d\hat{V}_U^{[\pm m]}}{dB_{\omega\mathbf{q}}^{\alpha}}, \hat{\rho}_0 \right]. \end{aligned}$$

The first and third terms in the above equation are the noninteracting and interacting terms found in the standard TDDFPT formulation within ALSDA<sup>95</sup>. The second and fourth terms are new, referred to as the noninteracting and interacting Hubbard terms, which arise from the Hubbard  $U$  correction. These four terms also appear in the dynamical resonant and antiresonant Sternheimer equations (11) and (12) with the respective signs of  $B_{\text{xc}}$  and  $m$ .

To evaluate the spin susceptibility tensor using Eq. (14), we can use the solution of Eq. (20). For practical computation using the Lanczos algorithm, it is convenient to rewrite Eqs. (14) and (20) as a resolvent of the Liouvillian:<sup>173</sup>

$$\chi_{\alpha\alpha'}(\mathbf{q}, \omega) = \langle \mathbf{w}_{\alpha} | (\omega - \hat{\mathcal{L}}_{\mathbf{q}})^{-1} | \mathbf{v}_{\alpha'} \rangle, \quad (22)$$

where  $\langle \mathbf{w}_\alpha | = \langle \{u_{n\mathbf{k}}\} | \mu_B \sigma_\alpha$  and  $|\mathbf{v}_{\alpha'}\rangle = [\frac{d\hat{V}_{\text{ext}}}{dB_{\omega\mathbf{q}}}, \hat{\rho}_0] |\{u_{n\mathbf{k}}\}\rangle$ , while  $\{u_{n\mathbf{k}}\}$  denotes a set of the ground-state KS wavefunctions. Next, we introduce the dual basis  $\{\langle \mathbf{p}_n |, |\mathbf{q}_n \rangle\}$  composed of “left”  $\langle \mathbf{p}_n |$  and “right”  $|\mathbf{q}_n \rangle$  Lanczos orthonormal vectors ( $\langle \mathbf{p}_n | \mathbf{q}_m \rangle = \delta_{n,m}$ ) that tridiagonalizes the Liouvillian:  $\langle \mathbf{p}_n | \hat{\mathcal{L}}_q | \mathbf{q}_m \rangle = \alpha_n \delta_{n,m} + \beta_n \delta_{n,m+1} + \gamma_n \delta_{n,m-1}$ , with  $n$  and  $m$  being integer numbers ( $n \geq 1, m \geq 1$ ). The Lanczos vectors are obtained by using the Lanczos recursive relations<sup>172</sup>:

$$\hat{\mathcal{L}}_q |\mathbf{q}_n\rangle = |\mathbf{q}_{n+1}\rangle \beta_{n+1} + |\mathbf{q}_n\rangle \alpha_n + |\mathbf{q}_{n-1}\rangle \gamma_n, \quad (23)$$

$$\hat{\mathcal{L}}_q^\dagger |\mathbf{p}_n\rangle = |\mathbf{p}_{n+1}\rangle \gamma_{n+1} + |\mathbf{p}_n\rangle \alpha_n + |\mathbf{p}_{n-1}\rangle \beta_n, \quad (24)$$

where  $\{\alpha_n \beta_n \gamma_n\}$  is a set of Lanczos coefficients that are defined as:  $\alpha_n = \langle \mathbf{p}_n | \hat{\mathcal{L}}_q | \mathbf{q}_n \rangle$ ,  $\beta_{n+1} = \sqrt{\langle \mathbf{u}_p | \mathbf{u}_q \rangle}$ , and  $\gamma_{n+1} = \beta_{n+1} \text{sign}[\langle \mathbf{u}_p | \mathbf{u}_q \rangle]$ , where  $|\mathbf{u}_q\rangle = |\mathbf{q}_{n+1}\rangle \beta_{n+1}$  and  $|\mathbf{u}_p\rangle = |\mathbf{p}_{n+1}\rangle \gamma_{n+1}$ <sup>95</sup>. By setting  $|\mathbf{p}_1\rangle = |\mathbf{q}_1\rangle = |\mathbf{v}_{\alpha'}\rangle$ , the resolvent of the Liouvillian in Eq. (22) can be expressed as a continued fraction<sup>103,117</sup>:

$$\chi_{\alpha\alpha'}(\mathbf{q}, \omega) = \frac{1}{\omega - \alpha_1 + \beta_2 \frac{1}{\omega - \alpha_2 + \dots} \gamma_2}. \quad (25)$$

In practice,  $\chi_{\alpha\alpha'}(\mathbf{q}, \omega)$  must be converged with respect to the number of Lanczos iterations  $n$  when solving Eqs. (23) and (24) recursively. Importantly, these equations are independent of the frequency  $\omega$ , meaning they need to be solved only once for each value of the transferred momentum  $\mathbf{q}$  and each  $\alpha$  Cartesian component of the external magnetic field. The frequency only comes into play in the post-processing step, using the Lanczos coefficients  $\{\alpha_n, \beta_n, \gamma_n\}$  to compute the spin susceptibility tensor according to Eq. (25). A small constant Lorentzian broadening  $\eta$  is added to the frequency  $\omega \rightarrow \omega + i\eta$  to regularize the cases when the frequency of the perturbation resonates with electronic vertical transition processes in the system (see the left-hand sides of Eqs. (11) and (12)). Since only the transverse component of  $\chi_{\alpha\alpha'}(\mathbf{q}, \omega)$  is needed to compute magnons, just one or two Lanczos chains are sufficient in some systems, depending on the system’s symmetry and the direction of the ground-state magnetization.

### Computational details

All calculations are performed using the QUANTUM ESPRESSO distribution<sup>174,175,161</sup>. The ground-

state calculations are carried out with the PW code<sup>174</sup> using LSDA<sup>176</sup> for the xc functional. Optimized norm-conserving scalar-relativistic pseudopotentials<sup>177</sup> are taken from the PSEUDO-DOJO library<sup>178</sup>. We use a 80 Ry kinetic-energy cutoff for the plane-wave expansion of the KS wavefunctions and a 320 Ry cutoff for the charge density. The BZ is sampled with a  $\Gamma$ -centered  $12 \times 12 \times 12$   $\mathbf{k}$ -points grid. The spin-orbit coupling is neglected.

The Hubbard  $U$  parameters are computed using DFPT<sup>57,59</sup> as implemented in the HP code<sup>179</sup>, with Löwdin-orthogonalized atomic orbitals for Hubbard projectors<sup>180</sup>. We employ uniform  $\Gamma$ -centered  $\mathbf{k}$ - and  $\mathbf{q}$ -point meshes of size  $8 \times 8 \times 8$  and  $4 \times 4 \times 4$ , respectively, and use kinetic-energy cutoffs of 90 Ry for the KS wavefunctions and 360 Ry for the charge density, providing an accuracy for the Hubbard parameters of  $\sim 0.01$  eV. The  $U$  parameters are computed iteratively in a self-consistent manner as described in Refs. 105,58, which includes Hubbard forces and stresses in DFT+ $U$  structural optimizations<sup>181</sup>.

The magnon energies are computed using TDDFPT+ $U$  and the LL approach, as implemented in a modified version of the TURBOMAGNON code<sup>182</sup>. We use ALSDA, both with and without Hubbard  $U$ . The TDDFPT and TDDFPT+ $U$  calculations are performed at their respective optimized rhombohedral lattice parameters reported in Table 1. The calculations employ the pseudo-Hermitian flavor of the Lanczos recursive algorithm<sup>2,12</sup>, which includes an extrapolation technique for the Lanczos coefficients<sup>173</sup>. A Gaussian smearing with a broadening parameter of 0.5 meV is used to plot the magnetic excitation spectra. All calculations are performed without symmetries since these are not yet implemented.

### DATA AVAILABILITY

The data used to produce the results of this work will be available in the Materials Cloud Archive prior to the publication at <https://archive.materialscloud.org>.

### CODE AVAILABILITY

The TURBOMAGNON code including Hubbard corrections is part of a customized version of QUANTUM ESPRESSO which will be made publicly available with the official future releases.

## ACKNOWLEDGEMENTS

We thank Tommaso Gorni and Flaviano dos Santos for fruitful discussions. We acknowledge support by the NCCR MARVEL, a National Centre of Competence in Research, funded by the Swiss National Science Foundation (Grant number 205602). L.B. acknowledges the Fellowship from the EPFL QSE Center "Many-body neural simulations of quantum materials" (grant number 10060). This work was supported by a grant from the Swiss National Supercomputing Centre (CSCS) under project ID s1073 and mr33 (Piz Daint).

## Author contributions statement

L.B. derived the equations and implemented the novel approach in QUANTUM ESPRESSO using preliminary I.T.'s routines. L.B. and I.T. tested the implementation and applied it to NiO and MnO. All the authors analysed the results and contributed to writing the manuscript.

## Competing interests

The authors declare no competing interests.

## References

1. Avsar, A. *et al.* Colloquium: Spintronics in graphene and other two-dimensional materials. *Rev. Mod. Phys.* **92**, 021003, DOI: [10.1103/RevModPhys.92.021003](https://doi.org/10.1103/RevModPhys.92.021003) (2020). Publisher: American Physical Society.
2. Gorni, T., Baseggio, O., Delugas, P., Timrov, I. & Baroni, S. First-principles study of the gap in the spin excitation spectrum of the  $\text{CrI}_3$  honeycomb ferromagnet. *Phys. Rev. B* **107**, L220410, DOI: [10.1103/PhysRevB.107.L220410](https://doi.org/10.1103/PhysRevB.107.L220410) (2023). Publisher: American Physical Society.
3. Ke, L. & Katsnelson, M. I. Electron correlation effects on exchange interactions and spin excitations in 2D van der Waals materials. *npj Comput. Mater.* **7**, 1–8, DOI: [10.1038/s41524-020-00469-2](https://doi.org/10.1038/s41524-020-00469-2) (2021). Publisher: Nature Publishing Group.
4. Šmejkal, L. *et al.* Chiral Magnons in Altermagnetic RuO<sub>2</sub>. *Phys. Rev. Lett.* **131**, 256703, DOI: [10.1103/PhysRevLett.131.256703](https://doi.org/10.1103/PhysRevLett.131.256703) (2023).
5. Cui, Q., Zeng, B., Cui, P., Yu, T. & Yang, H. Efficient spin Seebeck and spin Nernst effects of magnons in altermagnets. *Phys. Rev. B* **108**, L180401, DOI: [10.1103/PhysRevB.108.L180401](https://doi.org/10.1103/PhysRevB.108.L180401) (2023).
6. Leenders, R. A., Afanasiev, D., Kimel, A. & Mikhaylovskiy, R. Canted spin order as a platform for ultrafast conversion of magnons. *Nature* **630**, 335, DOI: [10.1038/s41586-024-07448-3](https://doi.org/10.1038/s41586-024-07448-3) (2024).
7. Costa, A. T., Henriques, J. & Fernández-Rossier, J. Giant spatial anisotropy of magnon lifetime in altermagnets. *arXiv:2405.12896* (2024).
8. Olsen, T. Unified Treatment of Magnons and Excitons in Monolayer  $\text{CrI}_3$  from Many-Body Perturbation Theory. *Phys. Rev. Lett.* **127**, 166402, DOI: [10.1103/PhysRevLett.127.166402](https://doi.org/10.1103/PhysRevLett.127.166402) (2021). Publisher: American Physical Society.
9. Bae, Y. J. *et al.* Exciton-coupled coherent magnons in a 2D semiconductor. *Nature* **609**, 282–286, DOI: [10.1038/s41586-022-05024-1](https://doi.org/10.1038/s41586-022-05024-1) (2022). Publisher: Nature Publishing Group.
10. Bistoni, O., Mauri, F. & Calandra, M. Intrinsic Vibrational Angular Momentum from Nonadiabatic Effects in Noncollinear Magnetic Molecules. *Phys. Rev. Lett.* **126**, 225703, DOI: [10.1103/PhysRevLett.126.225703](https://doi.org/10.1103/PhysRevLett.126.225703) (2021). Publisher: American Physical Society.
11. Bonini, J. *et al.* Frequency Splitting of Chiral Phonons from Broken Time-Reversal Symmetry in CrI<sub>3</sub>. *Phys. Rev. Lett.* **130**, 086701, DOI: [10.1103/PhysRevLett.130.086701](https://doi.org/10.1103/PhysRevLett.130.086701) (2023).
12. Delugas, P., Baseggio, O., Timrov, I., Baroni, S. & Gorni, T. Magnon-phonon interactions enhance the gap at the Dirac point in the spin-wave spectra of  $\text{CrI}_3$  two-dimensional magnets. *Phys. Rev. B* **107**, 214452, DOI: [10.1103/PhysRevB.107.214452](https://doi.org/10.1103/PhysRevB.107.214452) (2023). Publisher: American Physical Society.
13. Ren, S., Bonini, J., Stengel, M., Dreyer, C. E. & Vanderbilt, D. Adiabatic Dynamics of Coupled Spins and Phonons in Magnetic Insulators. *Phys. Rev. X* **14**, 011041, DOI: [10.1103/PhysRevX.14.011041](https://doi.org/10.1103/PhysRevX.14.011041) (2024). Pub-

lisher: American Physical Society.

14. Ghosh, S., Menichetti, G., Katsnelson, M. & Polini, M. Plasmon-magnon interactions in two-dimensional honeycomb magnets. *Phys. Rev. B* **107**, 195302, DOI: [10.1103/PhysRevB.107.195302](https://doi.org/10.1103/PhysRevB.107.195302) (2023).
15. Dyrdal, A., Qaiumzadeh, A., Brataas, A. & Barnaś, J. Magnon-plasmon hybridization mediated by spin-orbit interaction in magnetic materials. *Phys. Rev. B* **108**, 045414, DOI: [10.1103/PhysRevB.108.045414](https://doi.org/10.1103/PhysRevB.108.045414) (2023).
16. Falch, V., Danon, J., Qaiumzadeh, A. & Brataas, A. Impact of spin torques and spin-pumping phenomena on magnon-plasmon polaritons in antiferromagnetic insulator-semiconductor heterostructures. *Phys. Rev. B* **109**, 214436, DOI: [10.1103/PhysRevB.109.214436](https://doi.org/10.1103/PhysRevB.109.214436) (2024).
17. Imada, M., Fujimori, A. & Tokura, Y. Metal-insulator transitions. *Rev. Mod. Phys.* **70**, 1039, DOI: [10.1103/RevModPhys.70.1039](https://doi.org/10.1103/RevModPhys.70.1039) (1998).
18. Tóth, S. *et al.* Electromagnon dispersion probed by inelastic X-ray scattering in LiCrO<sub>2</sub>. *Nat. Commun.* **7**, 13547, DOI: [10.1038/ncomms13547](https://doi.org/10.1038/ncomms13547) (2016).
19. Pershoguba, S. *et al.* Dirac Magnons in Honeycomb Ferromagnets. *Phys. Rev. X* **8**, 011010, DOI: [10.1103/PhysRevX.8.011010](https://doi.org/10.1103/PhysRevX.8.011010) (2018).
20. Chen, L. *et al.* Topological Spin Excitations in Honeycomb Ferromagnet CrI<sub>3</sub>. *Phys. Rev. X* **8**, 041028, DOI: [10.1103/PhysRevX.8.041028](https://doi.org/10.1103/PhysRevX.8.041028) (2018).
21. Scheie, A. *et al.* Spin Waves and Magnetic Exchange Hamiltonian in CrSBr. *Adv. Sci.* **9**, 2202467, DOI: [10.1002/advs.202202467](https://doi.org/10.1002/advs.202202467) (2022).
22. Huang, C. *et al.* Extreme terahertz magnon multiplication induced by resonant magnetic pulse pairs. *Nat. Commun.* **15**, 3214, DOI: [10.1038/s41467-024-47471-6](https://doi.org/10.1038/s41467-024-47471-6) (2024).
23. Hohenberg, P. & Kohn, W. Inhomogeneous Electron Gas. *Phys. Rev.* **136**, B864–B871, DOI: [10.1103/PhysRev.136.B864](https://doi.org/10.1103/PhysRev.136.B864) (1964).
24. Kohn, W. & Sham, L. J. Self-Consistent Equations Including Exchange and Correlation Effects. *Phys. Rev.* **140**, A1133–A1138, DOI: [10.1103/PhysRev.140.A1133](https://doi.org/10.1103/PhysRev.140.A1133) (1965).
25. Lüders, M., Ernst, A., Temmerman, W., Szotek, Z. & Durham, P. Ab initio angle-resolved photoemission in multiple-scattering formulation. *J. Phys.: Condes. Matter* **13**, 8587, DOI: [10.1088/0953-8984/13/38/305](https://doi.org/10.1088/0953-8984/13/38/305) (2001).
26. Papanikolaou, N., Zeller, R. & Dederichs, P. Conceptual improvements of the KKR method. *J. Phys.: Condes. Matter* **14**, 2799, DOI: [10.1088/0953-8984/14/11/304](https://doi.org/10.1088/0953-8984/14/11/304) (2002).
27. Perdew, J. & Zunger, A. Self-interaction correction to density-functional approximations for many-electron systems. *Phys. Rev. B* **23**, 5048, DOI: [10.1103/PhysRevB.23.5048](https://doi.org/10.1103/PhysRevB.23.5048) (1981).
28. Mori-Sánchez, P., Cohen, A. & Yang, W. Many-electron self-interaction error in approximate density functionals. *J. Chem. Phys.* **125**, 201102, DOI: [10.1063/1.2403848](https://doi.org/10.1063/1.2403848) (2006).
29. Anisimov, V., Zaanen, J. & Andersen, O. Band theory and Mott insulators: Hubbard  $U$  instead of Stoner  $I$ . *Phys. Rev. B* **44**, 943, DOI: [10.1103/PhysRevB.44.943](https://doi.org/10.1103/PhysRevB.44.943) (1991).
30. Liechtenstein, A., Anisimov, V. & Zaanen, J. Density-functional theory and strong interactions: Orbital ordering in Mott-Hubbard insulators. *Phys. Rev. B* **52**, R5467, DOI: [10.1103/PhysRevB.52.R5467](https://doi.org/10.1103/PhysRevB.52.R5467) (1995).
31. Dudarev, S., Botton, G., Savrasov, S., Humphreys, C. & Sutton, A. Electron-energy-loss spectra and the structural stability of nickel oxide: An LSDA+ $U$  study. *Phys. Rev. B* **57**, 1505, DOI: [10.1103/PhysRevB.57.1505](https://doi.org/10.1103/PhysRevB.57.1505) (1998).
32. Kulik, H., Cococcioni, M., Scherlis, D. & Marzari, N. Density Functional Theory in Transition-Metal Chemistry: A Self-Consistent Hubbard  $U$  Approach. *Phys. Rev. Lett.* **97**, 103001, DOI: [10.1103/PhysRevLett.97.103001](https://doi.org/10.1103/PhysRevLett.97.103001) (2006).
33. Kulik, H. & Marzari, N. A self-consistent Hubbard  $U$  density-functional theory approach to the addition-elimination reactions of hydrocarbons on bare FeO<sup>+</sup>. *J. Chem. Phys.* **129**, 134314, DOI: [10.1063/1.2987444](https://doi.org/10.1063/1.2987444) (2008).
34. Dederichs, P., Blügel, S., Zeller, R. & Akai, H. Ground States of Constrained Systems: Application to Cerium Impurities. *Phys. Rev. Lett.* **53**, 2512, DOI: [10.1103/PhysRevLett.53.2512](https://doi.org/10.1103/PhysRevLett.53.2512) (1984).

35. McMahan, A., Martin, R. & Satpathy, S. Calculated effective Hamiltonian for  $\text{La}_2\text{CuO}_4$  and solution in the impurity Anderson approximation. *Phys. Rev. B* **38**, 6650, DOI: [10.1103/PhysRevB.38.6650](https://doi.org/10.1103/PhysRevB.38.6650) (1988).
36. Gunnarsson, O., Andersen, O., Jepsen, O. & Zaanen, J. Density-functional calculation of the parameters in the Anderson model: Application to Mn in CdTe. *Phys. Rev. B* **39**, 1708, DOI: [10.1103/PhysRevB.39.1708](https://doi.org/10.1103/PhysRevB.39.1708) (1989).
37. Hybertsen, M., Schlüter, M. & Christensen, N. Calculation of Coulomb-interaction parameters for  $\text{La}_2\text{CuO}_4$  using a constrained-density-functional approach. *Phys. Rev. B* **39**, 9028, DOI: [10.1103/PhysRevB.39.9028](https://doi.org/10.1103/PhysRevB.39.9028) (1989).
38. Gunnarsson, O. Calculation of parameters in model Hamiltonians. *Phys. Rev. B* **41**, 514, DOI: [10.1103/PhysRevB.41.514](https://doi.org/10.1103/PhysRevB.41.514) (1990).
39. Pickett, W., Erwin, S. & Ethridge, E. Reformulation of the LDA+ $U$  method for a local-orbital basis. *Phys. Rev. B* **58**, 1201, DOI: [10.1103/PhysRevB.58.1201](https://doi.org/10.1103/PhysRevB.58.1201) (1998).
40. Shishkin, M. & Sato, H. Self-consistent parametrization of DFT+ $U$  framework using linear response approach: Application to evaluation of redox potentials of battery cathodes. *Phys. Rev. B* **93**, 085135, DOI: [10.1103/PhysRevB.93.085135](https://doi.org/10.1103/PhysRevB.93.085135) (2016).
41. Mosey, N. & Carter, E. Ab initio evaluation of Coulomb and exchange parameters for DFT+ $U$  calculations. *Phys. Rev. B* **76**, 155123, DOI: [10.1103/PhysRevB.76.155123](https://doi.org/10.1103/PhysRevB.76.155123) (2007).
42. Mosey, N., Liao, P. & Carter, E. Rotationally invariant ab initio evaluation of Coulomb and exchange parameters for DFT+ $U$  calculations. *J. Chem. Phys.* **129**, 014103, DOI: [10.1063/1.2943142](https://doi.org/10.1063/1.2943142) (2008).
43. Andriotis, A., Sheetz, R. & Menon, M. LSDA+ $U$  method: A calculation of the  $U$  values at the Hartree-Fock level of approximation. *Phys. Rev. B* **81**, 245103, DOI: [10.1103/PhysRevB.81.245103](https://doi.org/10.1103/PhysRevB.81.245103) (2010).
44. Agapito, L., Curtarolo, S. & Buongiorno Nardelli, M. Reformulation of DFT+ $U$  as a Pseudohybrid Hubbard Density Functional for Accelerated Materials Discovery. *Phys. Rev. X* **5**, 011006, DOI: [10.1103/PhysRevX.5.011006](https://doi.org/10.1103/PhysRevX.5.011006) (2015).
45. Tancogne-Dejean, N. & Rubio, A. Parameter-free hybridlike functional based on an extended Hubbard model: DFT+ $U$ + $V$ . *Phys. Rev. B* **102**, 155117, DOI: [10.1103/PhysRevB.102.155117](https://doi.org/10.1103/PhysRevB.102.155117) (2020).
46. Lee, S.-H. & Son, Y.-W. First-principles approach with a pseudohybrid density functional for extended Hubbard interactions. *Phys. Rev. Res.* **2**, 043410, DOI: [10.1103/PhysRevResearch.2.043410](https://doi.org/10.1103/PhysRevResearch.2.043410) (2020).
47. Springer, M. & Aryasetiawan, F. Frequency-dependent screened interaction in Ni within the random-phase approximation. *Phys. Rev. B* **57**, 4364, DOI: [10.1103/PhysRevB.57.4364](https://doi.org/10.1103/PhysRevB.57.4364) (1998).
48. Kotani, T. *Ab initio* random-phase-approximation calculation of the frequency-dependent effective interaction between 3d electrons: Ni, Fe, and MnO. *J. Phys.: Condens. Matter* **12**, 2413, DOI: [10.1088/0953-8984/12/11/307](https://doi.org/10.1088/0953-8984/12/11/307) (2000).
49. Aryasetiawan, F. *et al.* Frequency-dependent local interactions and low-energy effective models from electronic structure calculations. *Phys. Rev. B* **70**, 195104, DOI: [10.1103/PhysRevB.70.195104](https://doi.org/10.1103/PhysRevB.70.195104) (2004).
50. Aryasetiawan, F., Karlsson, K., Jepsen, O. & Schönberger, U. Calculations of Hubbard  $U$  from first-principles. *Phys. Rev. B* **74**, 125106, DOI: [10.1103/PhysRevB.74.125106](https://doi.org/10.1103/PhysRevB.74.125106) (2006).
51. Yu, M., Yang, S., Wu, C. & Marom, N. Machine learning the Hubbard  $U$  parameter in DFT+ $U$  using Bayesian optimization. *npj Comput. Mater.* **6**, 180, DOI: [10.1038/s41524-020-00446-9](https://doi.org/10.1038/s41524-020-00446-9) (2020).
52. Yu, W. *et al.* Active Learning the High-Dimensional Transferable Hubbard  $U$  and  $V$  Parameters in the DFT+ $U$ + $V$  Scheme. *J. Chem. Theory Comput.* **19**, 6425, DOI: [10.1021/acs.jctc.2c01116](https://doi.org/10.1021/acs.jctc.2c01116) (2023).
53. Cai, G. *et al.* Predicting structure-dependent Hubbard  $U$  parameters via machine learning. *Mater. Futur.* **3**, 025601, DOI: [10.1088/2752-5724/ad19e2](https://doi.org/10.1088/2752-5724/ad19e2) (2024).
54. Uhrin, M., Zadoks, A., Binci, L., Marzari, N. & Timrov, I. Machine learning Hubbard parameters with equivariant neural networks. *submitted, arXiv:2406.02457* (2024).
55. Das, R. BMach: a Bayesian machine for opti-



- mizing Hubbard  $U$  parameters in DFT+ $U$  with machine learning. *arXiv:2407.20848* (2024).
56. Cococcioni, M. & de Gironcoli, S. Linear response approach to the calculation of the effective interaction parameters in the LDA +  $U$  method. *Phys. Rev. B* **71**, 035105, DOI: [10.1103/PhysRevB.71.035105](https://doi.org/10.1103/PhysRevB.71.035105) (2005).
  57. Timrov, I., Marzari, N. & Cococcioni, M. Hubbard parameters from density-functional perturbation theory. *Phys. Rev. B* **98**, 085127, DOI: [10.1103/PhysRevB.98.085127](https://doi.org/10.1103/PhysRevB.98.085127) (2018).
  58. Timrov, I., Marzari, N. & Cococcioni, M. Self-consistent Hubbard parameters from density-functional perturbation theory in the ultrasoft and projector-augmented wave formulations. *Phys. Rev. B* **103**, 045141, DOI: [10.1103/PhysRevB.103.045141](https://doi.org/10.1103/PhysRevB.103.045141) (2021).
  59. Binci, L. & Marzari, N. Noncollinear  $\mathit{DFT}+U$  and Hubbard parameters with fully relativistic ultrasoft pseudopotentials. *Phys. Rev. B* **108**, 115157, DOI: [10.1103/PhysRevB.108.115157](https://doi.org/10.1103/PhysRevB.108.115157) (2023). Publisher: American Physical Society.
  60. Ricca, C., Timrov, I., Cococcioni, M., Marzari, N. & Aschauer, U. Self-consistent site-dependent DFT+ $U$  study of stoichiometric and defective  $\mathit{SrMnO}_3$ . *Phys. Rev. B* **99**, 094102, DOI: [10.1103/PhysRevB.99.094102](https://doi.org/10.1103/PhysRevB.99.094102) (2019). Publisher: American Physical Society.
  61. Floris, A. *et al.* Hubbard-corrected density functional perturbation theory with ultrasoft pseudopotentials. *Phys. Rev. B* **101**, 064305, DOI: [10.1103/PhysRevB.101.064305](https://doi.org/10.1103/PhysRevB.101.064305) (2020).
  62. Zhou, J.-J. *et al.* Ab Initio Electron-Phonon Interactions in Correlated Electron Systems. *Phys. Rev. Lett.* **127**, 126404, DOI: [10.1103/PhysRevLett.127.126404](https://doi.org/10.1103/PhysRevLett.127.126404) (2021). Publisher: American Physical Society.
  63. Grassano, D., Binci, L. & Marzari, N. Type- $i$  antiferromagnetic weyl semimetal  $\mathit{InMnTe}_2$ . *Phys. Rev. Res.* **6**, 013140, DOI: [10.1103/PhysRevResearch.6.013140](https://doi.org/10.1103/PhysRevResearch.6.013140) (2024).
  64. Bonfà, P. *et al.* Magnetostriction-driven muon localisation in an antiferromagnetic oxide. *Phys. Rev. Lett.* **132**, 046701, DOI: [10.1103/PhysRevLett.132.046701](https://doi.org/10.1103/PhysRevLett.132.046701) (2024).
  65. Macke, E., Timrov, I., Marzari, N. & Ciacchi, L. C. Orbital-resolved dft+ $u$  for molecules and solids. *J. Chem. Theory Comput.* **20**, 4824–4843, DOI: [10.1021/acs.jctc.3c01403](https://doi.org/10.1021/acs.jctc.3c01403) (2024).
  66. Ponet, L., Di Lucente, E. & Marzari, N. The energy landscape of magnetic materials. *npj Comput. Mater.* **10**, DOI: [10.1038/s41524-024-01310-w](https://doi.org/10.1038/s41524-024-01310-w) (2024).
  67. Gelin, S. *et al.* Ternary oxides of  $s$ - and  $p$ -block metals for photocatalytic solar-to-hydrogen conversion. *PRX Energy* **3**, 013007, DOI: [10.1103/PRXEnergy.3.013007](https://doi.org/10.1103/PRXEnergy.3.013007) (2024).
  68. Chang, B. *et al.* First-Principles Electron-Phonon Interactions and Polarons in the Parent Cuprate  $\mathit{La}_2\mathit{CuO}_4$ . *arXiv:2401.11322* .
  69. Szilva, A. *et al.* Quantitative theory of magnetic interactions in solids. *Rev. Mod. Phys.* **95**, 035004, DOI: [10.1103/RevModPhys.95.035004](https://doi.org/10.1103/RevModPhys.95.035004) (2023). Publisher: American Physical Society.
  70. Šabani, D., Bacaksiz, C. & Milošević, M. V. Ab initio methodology for magnetic exchange parameters: Generic four-state energy mapping onto a Heisenberg spin Hamiltonian. *Phys. Rev. B* **102**, 014457, DOI: [10.1103/PhysRevB.102.014457](https://doi.org/10.1103/PhysRevB.102.014457) (2020).
  71. Halilov, S. V., Eschrig, H., Perlov, A. Y. & Oppeneer, P. M. Adiabatic spin dynamics from spin-density-functional theory: Application to Fe, Co, and Ni. *Phys. Rev. B* **58**, 293–302, DOI: [10.1103/PhysRevB.58.293](https://doi.org/10.1103/PhysRevB.58.293) (1998). Publisher: American Physical Society.
  72. Gebauer, R. & Baroni, S. Magnons in real materials from density-functional theory. *Phys. Rev. B* **61**, R6459–R6462, DOI: [10.1103/PhysRevB.61.R6459](https://doi.org/10.1103/PhysRevB.61.R6459) (2000).
  73. Jacobsson, A., Sanyal, B., Ležaić, M. & Blügel, S. Exchange parameters and adiabatic magnon energies from spin-spiral calculations. *Phys. Rev. B* **88**, 134427, DOI: [10.1103/PhysRevB.88.134427](https://doi.org/10.1103/PhysRevB.88.134427) (2013).
  74. Liechtenstein, A. I., Katsnelson, M. I., Antropov, V. P. & Gubanov, V. A. Local spin density functional approach to the theory of exchange interactions in ferromagnetic metals and alloys. *J. Magn. Magn. Mater.* **67**, 65–74, DOI: [10.1016/0304-8853\(87\)90721-9](https://doi.org/10.1016/0304-8853(87)90721-9) (1987).
  75. Solovyev, I., Hamada, N. & Terakura, K. Crucial Role of the Lattice Distortion in

- the Magnetism of LaMnO<sub>3</sub>. *Phys. Rev. Lett.* **76**, 4825–4828, DOI: [10.1103/PhysRevLett.76.4825](https://doi.org/10.1103/PhysRevLett.76.4825) (1996).
76. Pajda, M., Kudrnovský, J., Turek, I., Drchal, V. & Bruno, P. *Ab initio* calculations of exchange interactions, spin-wave stiffness constants, and Curie temperatures of Fe, Co, and Ni. *Phys. Rev. B* **64**, 174402, DOI: [10.1103/PhysRevB.64.174402](https://doi.org/10.1103/PhysRevB.64.174402) (2001).
  77. Korotin, D. M., Mazurenko, V. V., Anisimov, V. I. & Streltsov, S. V. Calculation of exchange constants of the Heisenberg model in plane-wave-based methods using the Green's function approach. *Phys. Rev. B* **91**, 224405, DOI: [10.1103/PhysRevB.91.224405](https://doi.org/10.1103/PhysRevB.91.224405) (2015).
  78. Bloch, F. Zur Theorie des Ferromagnetismus. *Z. Physik* **61**, 206, DOI: [10.1007/BF01339661](https://doi.org/10.1007/BF01339661) (1930).
  79. Slater, J. C. Cohesion in Monovalent Metals. *Phys. Rev.* **35**, 509, DOI: [10.1103/PhysRev.35.509](https://doi.org/10.1103/PhysRev.35.509) (1930).
  80. Holstein, T. & Primakoff, H. Field Dependence of the Intrinsic Domain Magnetization of a Ferromagnet. *Phys. Rev.* **58**, 1098, DOI: [10.1103/PhysRev.58.1098](https://doi.org/10.1103/PhysRev.58.1098) (1940).
  81. Zakeri, K., Zhang, Y., Chuang, T.-H. & Kirschner, J. Magnon lifetimes on the fe(110) surface: The role of spin-orbit coupling. *Phys. Rev. Lett.* **108**, 197205, DOI: [10.1103/PhysRevLett.108.197205](https://doi.org/10.1103/PhysRevLett.108.197205) (2012).
  82. Heinze, S. *et al.* Spontaneous atomic-scale magnetic skyrmion lattice in two dimensions. *Nat. Phys.* **7**, 713–718, DOI: [10.1038/nphys2045](https://doi.org/10.1038/nphys2045) (2011).
  83. Gross, E. K. U. & Kohn, W. Local density-functional theory of frequency-dependent linear response. *Phys. Rev. Lett.* **55**, 2850–2852, DOI: [10.1103/PhysRevLett.55.2850](https://doi.org/10.1103/PhysRevLett.55.2850) (1985). Publisher: American Physical Society.
  84. Hedin, L. New Method for Calculating the One-Particle Green's Function with Application to the Electron-Gas Problem. *Phys. Rev.* **139**, A796, DOI: [10.1103/PhysRev.139.A796](https://doi.org/10.1103/PhysRev.139.A796) (1965).
  85. Rousseau, B., Eiguren, A. & Bergara, A. Efficient computation of magnon dispersions within time-dependent density functional theory using maximally localized Wannier functions. *Phys. Rev. B* **85**, 054305, DOI: [10.1103/PhysRevB.85.054305](https://doi.org/10.1103/PhysRevB.85.054305) (2012). Publisher: American Physical Society.
  86. Lounis, S., Costa, A., Muniz, R. & Mills, D. Theory of local dynamical magnetic susceptibilities from the Korringa-Kohn-Rostoker Green function method. *Phys. Rev. B* **83**, 035109, DOI: [10.1103/PhysRevB.83.035109](https://doi.org/10.1103/PhysRevB.83.035109) (2011).
  87. Buczek, P., Ernst, A. & Sandratskii, L. Different dimensionality trends in the Landau damping of magnons in iron, cobalt, and nickel: Time-dependent density functional study. *Phys. Rev. B* **84**, 174418, DOI: [10.1103/PhysRevB.84.174418](https://doi.org/10.1103/PhysRevB.84.174418) (2011).
  88. dos Santos Dias, M., Schweglinghaus, B., Blügel, S. & Lounis, S. Relativistic dynamical spin excitations of magnetic adatoms. *Phys. Rev. B* **91**, 075405, DOI: [10.1103/PhysRevB.91.075405](https://doi.org/10.1103/PhysRevB.91.075405) (2015).
  89. Wysocki, A. *et al.* Spin-density fluctuations and the fluctuation-dissipation theorem in 3d ferromagnetic metals. *Phys. Rev. B* **96**, 184418, DOI: [10.1103/PhysRevB.96.184418](https://doi.org/10.1103/PhysRevB.96.184418) (2017).
  90. Singh, N., Elliott, P., Nautiyal, T., Dewhurst, J. & Sharma, S. Adiabatic generalized gradient approximation kernel in time-dependent density functional theory. *Phys. Rev. B* **99**, 035151, DOI: [10.1103/PhysRevB.99.035151](https://doi.org/10.1103/PhysRevB.99.035151) (2019).
  91. Skovhus, T. & Olsen, T. Dynamic transverse magnetic susceptibility in the projector augmented-wave method: Application to Fe, Ni, and Co. *Phys. Rev. B* **103**, 245110, DOI: [10.1103/PhysRevB.103.245110](https://doi.org/10.1103/PhysRevB.103.245110) (2021). Publisher: American Physical Society.
  92. Savrasov, S. Y. Linear Response Calculations of Spin Fluctuations. *Phys. Rev. Lett.* **81**, 2570–2573, DOI: [10.1103/PhysRevLett.81.2570](https://doi.org/10.1103/PhysRevLett.81.2570) (1998). Publisher: American Physical Society.
  93. Cao, K., Lambert, H., Radaelli, P. G. & Giustino, F. *Ab initio* calculation of spin fluctuation spectra using time-dependent density functional perturbation theory, plane waves, and pseudopotentials. *Phys. Rev. B* **97**, 024420, DOI: [10.1103/PhysRevB.97.024420](https://doi.org/10.1103/PhysRevB.97.024420) (2018).
  94. Liu, X., Lin, Y. & Feng, J. Implementation of

- the density functional perturbation theory for generalized susceptibility in the projector augmented wave framework. *Phys. Rev. B* **108**, 094405, DOI: [10.1103/PhysRevB.108.094405](https://doi.org/10.1103/PhysRevB.108.094405) (2023). Publisher: American Physical Society.
95. Gorni, T., Timrov, I. & Baroni, S. Spin dynamics from time-dependent density functional perturbation theory. *The Eur. Phys. J. B* **91**, 249, DOI: [10.1140/epjb/e2018-90247-9](https://doi.org/10.1140/epjb/e2018-90247-9) (2018).
  96. Tancogne-Dejean, N., Eich, F. G. & Rubio, A. Time-Dependent Magnons from First Principles. *J. Chem. Theory Comput.* **16**, 1007–1017, DOI: [10.1021/acs.jctc.9b01064](https://doi.org/10.1021/acs.jctc.9b01064) (2020). Publisher: American Chemical Society.
  97. Karlsson, K. & Aryasetiawan, F. Spin-wave excitation spectra of nickel and iron. *Phys. Rev. B* **62**, 3006–3009, DOI: [10.1103/PhysRevB.62.3006](https://doi.org/10.1103/PhysRevB.62.3006) (2000).
  98. Şaşıoğlu, E., Schindlmayr, A., Friedrich, C., Freimuth, F. & Blügel, S. Wannier-function approach to spin excitations in solids. *Phys. Rev. B* **81**, 054434, DOI: [10.1103/PhysRevB.81.054434](https://doi.org/10.1103/PhysRevB.81.054434) (2010). Publisher: American Physical Society.
  99. Müller, M. C. T. D., Blügel, S. & Friedrich, C. Electron-magnon scattering in elementary ferromagnets from first principles: Lifetime broadening and band anomalies. *Phys. Rev. B* **100**, 045130, DOI: [10.1103/PhysRevB.100.045130](https://doi.org/10.1103/PhysRevB.100.045130) (2019). Publisher: American Physical Society.
  100. Lee, C.-C., Hsueh, H. C. & Ku, W. Dynamical linear response of TDDFT with  $\text{LDA}+U$  functional: Strongly hybridized Frenkel excitons in NiO. *Phys. Rev. B* **82**, 081106, DOI: [10.1103/PhysRevB.82.081106](https://doi.org/10.1103/PhysRevB.82.081106) (2010). Publisher: American Physical Society.
  101. Orhan, O. K. & O'Regan, D. D. TDDFT + U : A critical assessment of the Hubbard U correction to exchange-correlation kernels and potentials. *Phys. Rev. B* **99**, 165120, DOI: [10.1103/PhysRevB.99.165120](https://doi.org/10.1103/PhysRevB.99.165120) (2019).
  102. Tancogne-Dejean, N., Oliveira, M. J. T. & Rubio, A. Self-consistent DFT + U method for real-space time-dependent density functional theory calculations. *Phys. Rev. B* **96**, 245133, DOI: [10.1103/PhysRevB.96.245133](https://doi.org/10.1103/PhysRevB.96.245133) (2017).
  103. Walker, B., Saitta, A. M., Gebauer, R. & Baroni, S. Efficient Approach to Time-Dependent Density-Functional Perturbation Theory for Optical Spectroscopy. *Phys. Rev. Lett.* **96**, 113001, DOI: [10.1103/PhysRevLett.96.113001](https://doi.org/10.1103/PhysRevLett.96.113001) (2006).
  104. Baroni, S., de Gironcoli, S., Dal Corso, A. & Giannozzi, P. Phonons and related crystal properties from density-functional perturbation theory. *Rev. Mod. Phys.* **73**, 515–562, DOI: [10.1103/RevModPhys.73.515](https://doi.org/10.1103/RevModPhys.73.515) (2001).
  105. Cococcioni, M. & Marzari, N. Energetics and cathode voltages of  $\text{LiMPO}_4$  olivines (M= $\text{Fe}$ ,  $\text{Mn}$ ) from extended Hubbard functionals. *Phys. Rev. Mater.* **3**, 033801, DOI: [10.1103/PhysRevMaterials.3.033801](https://doi.org/10.1103/PhysRevMaterials.3.033801) (2019). Publisher: American Physical Society.
  106. Baroni, S., Giannozzi, P. & Testa, A. Green's-function approach to linear response in solids. *Phys. Rev. Lett.* **58**, 1861–1864, DOI: [10.1103/PhysRevLett.58.1861](https://doi.org/10.1103/PhysRevLett.58.1861) (1987).
  107. Rocca, D., Gebauer, R., Saad, Y. & Baroni, S. Turbo charging time-dependent density-functional theory with Lanczos chains. *The J. Chem. Phys.* **128**, 154105, DOI: [10.1063/1.2899649](https://doi.org/10.1063/1.2899649) (2008).
  108. Timrov, I., Vast, N., Gebauer, R. & Baroni, S. Electron energy loss and inelastic x-ray scattering cross sections from time-dependent density-functional perturbation theory. *Phys. Rev. B* **88**, 064301, DOI: [10.1103/PhysRevB.88.064301](https://doi.org/10.1103/PhysRevB.88.064301) (2013).
  109. Floris, A., De Gironcoli, S., Gross, E. K. U. & Cococcioni, M. Vibrational properties of MnO and NiO from DFT + U -based density functional perturbation theory. *Phys. Rev. B* **84**, 161102, DOI: [10.1103/PhysRevB.84.161102](https://doi.org/10.1103/PhysRevB.84.161102) (2011).
  110. Zhu, X., Edström, A. & Ederer, C. Magnetic exchange interactions in  $\text{SrMnO}_3$ . *Phys. Rev. B* **101**, 064401, DOI: [10.1103/PhysRevB.101.064401](https://doi.org/10.1103/PhysRevB.101.064401) (2020).
  111. Wan, X., Yin, Q. & Savrasov, S. Y. Calculation of Magnetic Exchange Interactions in Mott-Hubbard Systems. *Phys. Rev. Lett.* **97**, 266403, DOI: [10.1103/PhysRevLett.97.266403](https://doi.org/10.1103/PhysRevLett.97.266403) (2006). Publisher: American Physical Society.
  112. Kotani, T. & Schilfsgaarde, M. v. Spin

- wave dispersion based on the quasiparticle self-consistent GW method: NiO, MnO and  $\alpha$ -MnAs. *J. Physics: Condens. Matter* **20**, 295214, DOI: [10.1088/0953-8984/20/29/295214](https://doi.org/10.1088/0953-8984/20/29/295214) (2008).
113. Gonze, X. & Lee, C. Dynamical matrices, Born effective charges, dielectric permittivity tensors, and interatomic force constants from density-functional perturbation theory. *Phys. Rev. B* **55**, 10355–10368, DOI: [10.1103/PhysRevB.55.10355](https://doi.org/10.1103/PhysRevB.55.10355) (1997). Publisher: American Physical Society.
  114. Urru, A. & Dal Corso, A. Density functional perturbation theory for lattice dynamics with fully relativistic ultrasoft pseudopotentials: The magnetic case. *Phys. Rev. B* **100**, 045115, DOI: [10.1103/PhysRevB.100.045115](https://doi.org/10.1103/PhysRevB.100.045115) (2019).
  115. Vanderbilt, D. Soft self-consistent pseudopotentials in a generalized eigenvalue formalism. *Phys. Rev. B* **41**, 7892–7895, DOI: [10.1103/PhysRevB.41.7892](https://doi.org/10.1103/PhysRevB.41.7892) (1990).
  116. Blöchl, P. E. Projector augmented-wave method. *Phys. Rev. B* **50**, 17953–17979, DOI: [10.1103/PhysRevB.50.17953](https://doi.org/10.1103/PhysRevB.50.17953) (1994).
  117. Walker, B. & Gebauer, R. Ultrasoft pseudopotentials in time-dependent density-functional theory. *The J. Chem. Phys.* **127**, 164106, DOI: [10.1063/1.2786999](https://doi.org/10.1063/1.2786999) (2007).
  118. Motornyi, O. *et al.* Electron energy loss spectroscopy of bulk gold with ultrasoft pseudopotentials and the Liouville-Lanczos method. *Phys. Rev. B* **102**, 035156, DOI: [10.1103/PhysRevB.102.035156](https://doi.org/10.1103/PhysRevB.102.035156) (2020).
  119. Dudarev, S. L. *et al.* Parametrization of LSDA + U for noncollinear magnetic configurations: Multipolar magnetism in UO<sub>2</sub>. *Phys. Rev. Mater.* **3**, 083802, DOI: [10.1103/PhysRevMaterials.3.083802](https://doi.org/10.1103/PhysRevMaterials.3.083802) (2019).
  120. Savrasov, S. Y. & Kotliar, G. Ground State Theory of d-Pu. *Phys. Rev. Lett.* **84** (2000).
  121. Sakurai, J. J. & Napolitano, J. *Modern Quantum Mechanics* (Cambridge University Press, Cambridge, 2020), 3 edn.
  122. Cococcioni, M. Accurate and Efficient Calculations on Strongly Correlated Minerals with the LDA+U Method: Review and Perspectives. *Rev. Mineral. Geochem.* **71**, 147–167, DOI: [10.2138/rmg.2010.71.8](https://doi.org/10.2138/rmg.2010.71.8) (2010).
  123. de Gironcoli, S. Lattice dynamics of metals from density-functional perturbation theory. *Phys. Rev. B* **51**, 6773–6776, DOI: [10.1103/PhysRevB.51.6773](https://doi.org/10.1103/PhysRevB.51.6773) (1995).
  124. Calandra, M., Profeta, G. & Mauri, F. Adiabatic and nonadiabatic phonon dispersion in a Wannier function approach. *Phys. Rev. B* **82**, 165111, DOI: [10.1103/PhysRevB.82.165111](https://doi.org/10.1103/PhysRevB.82.165111) (2010). Publisher: American Physical Society.
  125. Giustino, F., Cohen, M. L. & Louie, S. G. GW method with the self-consistent Sternheimer equation. *Phys. Rev. B* **81**, 115105, DOI: [10.1103/PhysRevB.81.115105](https://doi.org/10.1103/PhysRevB.81.115105) (2010). Publisher: American Physical Society.
  126. Binci, L., Barone, P. & Mauri, F. First-principles theory of infrared vibrational spectroscopy of metals and semimetals: Application to graphite. *Phys. Rev. B* **103**, 134304, DOI: [10.1103/PhysRevB.103.134304](https://doi.org/10.1103/PhysRevB.103.134304) (2021). Publisher: American Physical Society.
  127. Baroni, S. & Gebauer, R. *Fundamentals of Time-Dependent Density Functional Theory*, chap. 19-The Liouville-Lanczos Approach to Time-Dependent Density-Functional Perturbation Theory, 375–390 (Springer, Berlin, 2012).
  128. Srinivasan, G. & Seehra, M. Magnetic susceptibilities, their temperature variation, and exchange constants of NiO. *Phys. Rev. B* **29**, 6295, DOI: [10.1103/PhysRevB.29.6295](https://doi.org/10.1103/PhysRevB.29.6295) (1984).
  129. Blech, I. & Averbach, B. Spin correlations in MnO. *Physics* **1**, 31 (1964).
  130. Schmahl, N., Barthel, J. & Eikerling, G. *Z. Anorg. Allg. Chem.* **332**, 230, DOI: [10.1002/zaac.19643320503](https://doi.org/10.1002/zaac.19643320503) (1964).
  131. Sasaki, S., Fujino, K., Taki-Uchi, Y. & Sadanag, R. *Acta Cryst. A* **36**, 904, DOI: [10.1107/S0567739480001908](https://doi.org/10.1107/S0567739480001908) (1980).
  132. Fender, B., Jacobson, A. & Wedgwood, F. *J. Chem. Phys.* **48**, 990, DOI: [10.1063/1.1668855](https://doi.org/10.1063/1.1668855) (1968).
  133. Cheetham, A. & Hope, D. *Phys. Rev. B* **27**, 6964, DOI: [10.1103/PhysRevB.27.6964](https://doi.org/10.1103/PhysRevB.27.6964) (1983).
  134. Kurmaev, E. *et al.* *Phys. Rev. B* **77**, 165127, DOI: [10.1103/PhysRevB.77.165127](https://doi.org/10.1103/PhysRevB.77.165127) (2008).
  135. Sawatzky, G. & Allen, J. *Phys. Rev. Lett.* **53**, 2339, DOI: [10.1103/PhysRevLett.53.2339](https://doi.org/10.1103/PhysRevLett.53.2339)

- (1984).
136. van Elp, J., Potze, R., Eskes, H., Berger, R. & Sawatzky, G. *Phys. Rev. B* **44**, 1530, DOI: [10.1103/PhysRevB.44.1530](https://doi.org/10.1103/PhysRevB.44.1530) (1991).
  137. Perdew, J. P. *et al.* Restoring the Density-Gradient Expansion for Exchange in Solids and Surfaces. *Phys. Rev. Lett.* **100**, 136406, DOI: [10.1103/PhysRevLett.100.136406](https://doi.org/10.1103/PhysRevLett.100.136406) (2008).
  138. Sun, J., Ruzsinszky, A. & Perdew, J. Strongly Constrained and Appropriately Normed Semilocal Density Functional. *Phys. Rev. Lett.* **115**, 036402, DOI: [10.1103/PhysRevLett.115.036402](https://doi.org/10.1103/PhysRevLett.115.036402) (2015).
  139. Kirchner-Hall, N., Zhao, W., Xiong, Y., Timrov, I. & Dabo, I. Extensive Benchmarking of DFT+ $U$  Calculations for Predicting Band Gaps. *Appl. Sci.* **11**, 2395, DOI: [10.3390/app11052395](https://doi.org/10.3390/app11052395) (2021).
  140. Lambert, D. S. & O'Regan, D. D. Use of DFT+ $U$ + $J$  with linear response parameters to predict non-magnetic oxide band gaps with hybrid-functional accuracy. *Phys. Rev. Res.* **5**, 013160, DOI: [10.1103/PhysRevResearch.5.013160](https://doi.org/10.1103/PhysRevResearch.5.013160) (2023).
  141. Leiria Campo Jr, V. & Cococcioni, M. Extended DFT +  $U$  +  $V$  method with on-site and inter-site electronic interactions. *J. Physics: Condens. Matter* **22**, 055602, DOI: [10.1088/0953-8984/22/5/055602](https://doi.org/10.1088/0953-8984/22/5/055602) (2010).
  142. van Setten, M. J. *et al.* Gw100: Benchmarking g0w0 for molecular systems. *J. Chem. Theory Comput.* **11**, 5665–5687, DOI: [10.1021/acs.jctc.5b00453](https://doi.org/10.1021/acs.jctc.5b00453) (2015).
  143. Grumet, M., Liu, P., Kaltak, M., Klimeš, J. c. v. & Kresse, G. Beyond the quasiparticle approximation: Fully self-consistent  $gw$  calculations. *Phys. Rev. B* **98**, 155143, DOI: [10.1103/PhysRevB.98.155143](https://doi.org/10.1103/PhysRevB.98.155143) (2018).
  144. Bonacci, M. *et al.* Towards high-throughput many-body perturbation theory: efficient algorithms and automated workflows. *npj Comput. Mater.* **9**, DOI: [10.1038/s41524-023-01027-2](https://doi.org/10.1038/s41524-023-01027-2) (2023).
  145. Wing, D. *et al.* Band gaps of crystalline solids from Wannier-localization-based optimal tuning of a screened range-separated hybrid functional. *Proc. Natl. Acad. Sci.* **118**, e2104556118, DOI: [10.1073/pnas.2104556118](https://doi.org/10.1073/pnas.2104556118) (2021).
  146. Skone, J. H., Govoni, M. & Galli, G. Nonempirical range-separated hybrid functionals for solids and molecules. *Phys. Rev. B* **93**, 235106, DOI: [10.1103/PhysRevB.93.235106](https://doi.org/10.1103/PhysRevB.93.235106) (2016).
  147. Chen, W., Miceli, G., Rignanese, G.-M. & Pasquarello, A. Nonempirical dielectric-dependent hybrid functional with range separation for semiconductors and insulators. *Phys. Rev. Mater.* **2**, 073803, DOI: [10.1103/PhysRevMaterials.2.073803](https://doi.org/10.1103/PhysRevMaterials.2.073803) (2018).
  148. Dabo, I. *et al.* Koopmans' Condition for Density-Functional Theory. *Phys. Rev. B* **82**, 115121, DOI: [10.1103/PhysRevB.82.115121](https://doi.org/10.1103/PhysRevB.82.115121) (2010).
  149. Nguyen, N. L., Colonna, N., Ferretti, A. & Marzari, N. Koopmans-Compliant Spectral Functionals for Extended Systems. *Phys. Rev. X* **8**, 021051, DOI: [10.1103/PhysRevX.8.021051](https://doi.org/10.1103/PhysRevX.8.021051) (2018).
  150. Linscott, E. B. *et al.* Koopmans : An Open-Source Package for Accurately and Efficiently Predicting Spectral Properties with Koopmans Functionals. *J. Chem. Theory Comput.* **19**, 7097, DOI: [10.1021/acs.jctc.3c00652](https://doi.org/10.1021/acs.jctc.3c00652) (2023).
  151. Van Hove, L. Correlations in Space and Time and Born Approximation Scattering in Systems of Interacting Particles. *Phys. Rev.* **95**, 249–262, DOI: [10.1103/PhysRev.95.249](https://doi.org/10.1103/PhysRev.95.249) (1954). Publisher: American Physical Society.
  152. Blume, M. Polarization Effects in the Magnetic Elastic Scattering of Slow Neutrons. *Phys. Rev.* **130**, 1670–1676, DOI: [10.1103/PhysRev.130.1670](https://doi.org/10.1103/PhysRev.130.1670) (1963). Publisher: American Physical Society.
  153. Malcioğlu, O. B., Gebauer, R., Rocca, D. & Baroni, S. turboTDDFT – A code for the simulation of molecular spectra using the Liouville–Lanczos approach to time-dependent density-functional perturbation theory. *Comput. Phys. Commun.* **182**, 1744–1754, DOI: [10.1016/j.cpc.2011.04.020](https://doi.org/10.1016/j.cpc.2011.04.020) (2011).
  154. Hutchings, M. T. & Samuelsen, E. J. Measurement of Spin-Wave Dispersion in NiO by Inelastic Neutron Scattering and Its Relation to Magnetic Properties. *Phys. Rev. B* **6**, 3447–3461, DOI: [10.1103/PhysRevB.6.3447](https://doi.org/10.1103/PhysRevB.6.3447) (1972).
  155. Pepy, G. Spin waves in MnO; from 4°K to

- temperatures close to  $T_N$ . *J. Phys. Chem. Solids* **35**, 433–444, DOI: [10.1016/S0022-3697\(74\)80037-5](https://doi.org/10.1016/S0022-3697(74)80037-5) (1974).
156. Fischer, G. *et al.* Exchange coupling in transition metal monoxides: Electronic structure calculations. *Phys. Rev. B* **80**, 014408, DOI: [10.1103/PhysRevB.80.014408](https://doi.org/10.1103/PhysRevB.80.014408) (2009).
  157. Lines, M. E. & Jones, E. D. Antiferromagnetism in the Face-Centered Cubic Lattice. II. Magnetic Properties of MnO. *Phys. Rev.* **139**, A1313–A1327, DOI: [10.1103/PhysRev.139.A1313](https://doi.org/10.1103/PhysRev.139.A1313) (1965).
  158. Kohgi, M., Ishikawa, Y. & Endoh, Y. Inelastic neutron scattering study of spin waves in MnO. *Solid State Commun.* **11**, 391, DOI: [10.1016/0038-1098\(72\)90255-4](https://doi.org/10.1016/0038-1098(72)90255-4) (1972).
  159. dos Santos, F. *et al.* *preparation* (2024).
  160. Tancogne-Dejean, N., Sentef, M. A. & Rubio, A. Ultrafast Modification of Hubbard  $U$  in a Strongly Correlated Material: Ab initio High-Harmonic Generation in NiO. *Phys. Rev. Lett.* **121**, 097402, DOI: [10.1103/PhysRevLett.121.097402](https://doi.org/10.1103/PhysRevLett.121.097402) (2018). Publisher: American Physical Society.
  161. Giannozzi, P. *et al.* Quantum ESPRESSO toward the exascale. *J. Chem. Phys.* **152**, 154105, DOI: [10.1063/5.0005082](https://doi.org/10.1063/5.0005082) (2020).
  162. Carnimeo, I. *et al.* Quantum ESPRESSO: One Further Step toward the Exascale. *J. Chem. Theory Comput.* **19**, 6292, DOI: [10.1021/acs.jctc.3c00249](https://doi.org/10.1021/acs.jctc.3c00249) (2023).
  163. Timrov, I. *et al.* Electronic structure of Ni-substituted LaFeO<sub>3</sub> from near edge x-ray absorption fine structure experiments and first-principles simulations. *Phys. Rev. Res.* **2**, 033265, DOI: [10.1103/PhysRevResearch.2.033265](https://doi.org/10.1103/PhysRevResearch.2.033265) (2020).
  164. Mahajan, R., Timrov, I., Marzari, N. & Kashyap, A. Importance of intersite Hubbard interactions in  $\beta$ -MnO<sub>2</sub>: A first-principles DFT+ $U$ + $V$  study. *Phys. Rev. Mater.* **5**, 104402, DOI: [10.1103/PhysRevMaterials.5.104402](https://doi.org/10.1103/PhysRevMaterials.5.104402) (2021).
  165. Mahajan, R., Kashyap, A. & Timrov, I. Pivotal Role of Intersite Hubbard Interactions in Fe-Doped  $\alpha$ -MnO<sub>2</sub>. *J. Phys. Chem. C* **126**, 14353, DOI: <https://doi.org/10.1021/acs.jpcc.2c04767> (2022).
  166. Timrov, I., Aquilante, F., Cococcioni, M. & Marzari, N. Accurate Electronic Properties and Intercalation Voltages of Olivine-type Li-ion Cathode Materials from Extended Hubbard Functionals. *PRX Energy* **1**, 033003, DOI: [10.1103/PRXEnergy.1.033003](https://doi.org/10.1103/PRXEnergy.1.033003) (2022).
  167. Timrov, I., Kotiuga, M. & Marzari, N. Unraveling the effects of inter-site Hubbard interactions in spinel Li-ion cathode materials. *Phys. Chem. Chem. Phys.* **25**, 9061, DOI: [10.1039/d3cp00419h](https://doi.org/10.1039/d3cp00419h) (2023).
  168. Binci, L., Kotiuga, M., Timrov, I. & Marzari, N. Hybridization driving distortions and multiferroicity in rare-earth nickelates. *Phys. Rev. Res.* **5**, 033146, DOI: [10.1103/PhysRevResearch.5.033146](https://doi.org/10.1103/PhysRevResearch.5.033146) (2023).
  169. Gebreyesus, G., Bastonero, L., Kotiuga, M., Marzari, N. & Timrov, I. Understanding the role of Hubbard corrections in the rhombohedral phase of BaTiO<sub>3</sub>. *Phys. Rev. B* **108**, 235171, DOI: [10.1103/PhysRevB.108.235171](https://doi.org/10.1103/PhysRevB.108.235171) (2023).
  170. Haddadi, F., Linscott, E., Timrov, I., Marzari, N. & Gibertini, M. On-site and inter-site Hubbard corrections in magnetic monolayers: The case of FePS<sub>3</sub> and CrI<sub>3</sub>. *Phys. Rev. Mater.* **8**, 014007, DOI: [10.1103/PhysRevMaterials.8.014007](https://doi.org/10.1103/PhysRevMaterials.8.014007) (2024).
  171. Huber, S. P. *et al.* AiiDA 1.0, a scalable computational infrastructure for automated reproducible workflows and data provenance. *Sci. Data* **7**, 300, DOI: [10.1038/s41597-020-00638-4](https://doi.org/10.1038/s41597-020-00638-4) (2020).
  172. Saad, Y. *Iterative Methods for Sparse Linear Systems* (SIAM, Philadelphia, 2003), 2nd edn.
  173. Rocca, D., Gebauer, R., Saad, Y. & Baroni, S. Turbo charging time-dependent density-functional theory with Lanczos chains. *J. Chem. Phys.* **128**, 154105, DOI: [10.1063/1.2899649](https://doi.org/10.1063/1.2899649) (2008).
  174. Giannozzi, P. *et al.* QUANTUM ESPRESSO: a modular and open-source software project for quantum simulations of materials. *J. Physics: Condens. Matter* **21**, 395502, DOI: [10.1088/0953-8984/21/39/395502](https://doi.org/10.1088/0953-8984/21/39/395502) (2009).
  175. Giannozzi, P. *et al.* Advanced capabilities for materials modelling with Quantum ESPRESSO. *J. Physics: Condens. Matter* **29**, 465901, DOI: [10.1088/1361-648X/aa8f79](https://doi.org/10.1088/1361-648X/aa8f79)

- (2017).
176. Perdew, J. P. & Wang, Y. Accurate and simple analytic representation of the electron-gas correlation energy. *Phys. Rev. B* **45**, 13244–13249, DOI: [10.1103/PhysRevB.45.13244](https://doi.org/10.1103/PhysRevB.45.13244) (1992). Publisher: American Physical Society.
  177. Hamann, D. R. Optimized norm-conserving Vanderbilt pseudopotentials. *Phys. Rev. B* **88**, 085117, DOI: [10.1103/PhysRevB.88.085117](https://doi.org/10.1103/PhysRevB.88.085117) (2013).
  178. Van Setten, M. *et al.* The PseudoDojo: Training and grading a 85 element optimized norm-conserving pseudopotential table. *Comput. Phys. Commun.* **226**, 39–54, DOI: [10.1016/j.cpc.2018.01.012](https://doi.org/10.1016/j.cpc.2018.01.012) (2018).
  179. Timrov, I., Marzari, N. & Cococcioni, M. HP – A code for the calculation of Hubbard parameters using density-functional perturbation theory. *Comput. Phys. Commun.* **279**, 108455, DOI: [10.1016/j.cpc.2022.108455](https://doi.org/10.1016/j.cpc.2022.108455) (2022).
  180. Löwdin, P.-O. On the Non-Orthogonality Problem Connected with the Use of Atomic Wave Functions in the Theory of Molecules and Crystals. *J. Chem. Phys.* **18**, 365, DOI: [10.1063/1.1747632](https://doi.org/10.1063/1.1747632) (1950).
  181. Timrov, I., Aquilante, F., Binci, L., Cococcioni, M. & Marzari, N. Pulay forces in density-functional theory with extended Hubbard functionals: From nonorthogonalized to orthogonalized manifolds. *Phys. Rev. B* **102**, 235159, DOI: [10.1103/PhysRevB.102.235159](https://doi.org/10.1103/PhysRevB.102.235159) (2020).
  182. Gorni, T., Baseggio, O., Delugas, P., Baroni, S. & Timrov, I. turboMagnon – A code for the simulation of spin-wave spectra using the Liouville-Lanczos approach to time-dependent density-functional perturbation theory. *Comput. Phys. Commun.* **280**, 108500, DOI: [10.1016/j.cpc.2022.108500](https://doi.org/10.1016/j.cpc.2022.108500) (2022).